Available online at www.sciencedirect.com
ScienceDirect
Geochimica et Cosmochimica Acta 73 (2009) 2769–2803
Geochimica et Cosmochimica Acta
www.elsevier.com/locate/gca

Chemical weathering of a marine terrace chronosequence, Santa Cruz, California. Part II: Solute profiles, gradients and the comparisons of contemporary and long-term weathering rates

Art F. White [a,*], Marjorie S. Schulz [a], David A. Stonestrom [a], Davison V. Vivit [a], John Fitzpatrick [a], Tom D. Bullen [a], Kate Maher [b], Alex E. Blum [c]

[a] U.S. Geological Survey, Menlo Park, CA 94025, USA
[b] Department of Geological and Environmental Sciences, Stanford University, Stanford, CA 94305, USA
[c] U.S. Geological Survey, Boulder 80303, CO, USA

Received 30 April 2008; accepted in revised form 28 January 2009; available online 14 February 2009

Abstract

The spatial and temporal changes in hydrology and pore water elemental and $^{87}Sr/^{86}Sr$ compositions are used to determine contemporary weathering rates in a 65- to 226-kyr-old soil chronosequence formed from granitic sediments deposited on marine terraces along coastal California. Soil moisture, tension and saturation exhibit large seasonal variations in shallow soils in response to a Mediterranean climate. These climate effects are dampened in underlying argillic horizons that progressively developed in older soils, and reached steady-state conditions in unsaturated horizons extending to depths in excess of 15 m. Hydraulic fluxes (q_h), based on Cl mass balances, vary from 0.06 to 0.22 m yr^{-1}, resulting in fluid residence times in the terraces of 10–24 yrs.

As expected for a coastal environment, the order of cation abundances in soil pore waters is comparable to sea water, i.e., $Na > Mg > Ca > K > Sr$, while the anion sequence $Cl > NO_3 > HCO_3 > SO_4$ reflects modifying effects of nutrient cycling in the grassland vegetation. Net Cl-corrected solute Na, K and Si increase with depth, denoting inputs from feldspar weathering. Solute $^{87}Sr/^{86}Sr$ ratios exhibit progressive mixing of sea water-dominated precipitation with inputs from less radiogenic plagioclase. While net Sr and Ca concentrations are anomalously high in shallow soils due to biological cycling, they decline with depth to low and/or negative net concentrations. Ca/Mg, Sr/Mg and $^{87}Sr/^{86}Sr$ solute and exchange ratios are similar in all the terraces, denoting active exchange equilibration with selectivities close to unity for both detrital smectite and secondary kaolinite. Large differences in the magnitudes of the pore waters and exchange reservoirs result in short-term buffering of the solute Ca, Sr, and Mg. Such buffering over geologic time scales can not be sustained due to declining inputs from residual plagioclase and smectite, implying periodic resetting of the exchange reservoir such as by past vegetational changes and/or climate.

Pore waters approach thermodynamic saturation with respect to albite at depth in the younger terraces, indicating that weathering rates ultimately become transport-limited and dependent on hydrologic flux. Contemporary rates R_{solute} are estimated from linear Na and Si pore weathering gradients b_{solute} such that

$$R_{solute} = \frac{q_h}{b_{solute}\beta S_v}$$

where S_v is the volumetric surface area and β is the stoichiometric coefficient. Plagioclase weathering rates ($0.38–2.8 \times 10^{-15}$ mol m^{-2} s^{-1}) are comparable to those based on $^{87}Sr/^{86}Sr$ mass balances and solid-state Na and Ca gradients using analogous gradient approximations. In addition, contemporary solute gradients, under transport-limited conditions, approximate long-term solid-state gradients when normalized against the mass of protolith plagioclase and its corresponding

* Corresponding author. Fax: +1 650 329 4538.
E-mail address: afwhite@usgs.gov (A.F. White).

0016-7037/$ - see front matter Published by Elsevier Ltd.
doi:10.1016/j.gca.2009.01.029

aqueous solubility. The multi-faceted weathering analysis presented in this paper is perhaps the most comprehensive yet applied to a single field study. Within uncertainties of the methods used, present day weathering rates, based on solute characterizations, are comparable to average long-term past rates as evidenced by soil profiles.
Published by Elsevier Ltd.

1. INTRODUCTION

A significant body of research has employed solid-state physical and chemical characteristics of chronosequence members to provide "snapshots in time" of weathering processes and to describe how weathering rates affect the long-term evolution of soils. In a further extension of this effort, White et al. (2008) presented a detailed description of a soil chronosequence developed on a series of marine terraces near Santa Cruz California. That paper described primary and secondary mineralogy and elemental distributions, characterized weathering profile development over time and proposed methods for calculating long-term weathering rates based on soil profile geometries.

In contrast to such solid-state characterization, fewer studies have described the hydrologic and solute characteristics of soil chronosequences, determined how these features progressively evolved with increasing soil age, or characterized the relationship between solute weathering rates and the observed mineral and element distributions in the soils (Chadwick et al., 2003; White et al., 2005). The current paper describes hydrochemical processes in the Santa Cruz terraces, and along with a companion paper in this volume (Maher et al., 2009), investigates solute controls on rates of chemical weathering.

The geology, geomorphology, mineralogy and ages of the Santa Cruz terraces are described in White et al. (2008). Briefly, the chronosequence involves a series of five successively elevated marine terraces situated adjacent to the Pacific Ocean, approximately 110 km SW of San Francisco (Fig. 1). A number of studies have provided age estimates of the terraces with the most recent, based on ^{10}Be, producing ages of between 65 and 226 kyrs. (Perg et al., 2001). The terraces began as wave cut platforms during high stands of sea level. Sediments deposited on these platforms consisted of beach sands, finer grained near-shore sediments and thin surficial eolian deposits (Bradley and Griggs, 1976; Anderson et al., 1999). Platform formation was accompanied by tectonic uplift, which eventually stranded the terrace sediments above subsequent marine high stands. Today, the area experiences a Mediterranean climate with mild wet winters and warm dry summers. The terraces are dominated by California coastal grass prairies interspersed with oak woodlands.

2. METHODS

Instrumented sites were developed on each of the 5 Santa Cruz terraces (Fig. 1) with selection criteria described in White et al. (2008). Hydrochemical measurements at all the

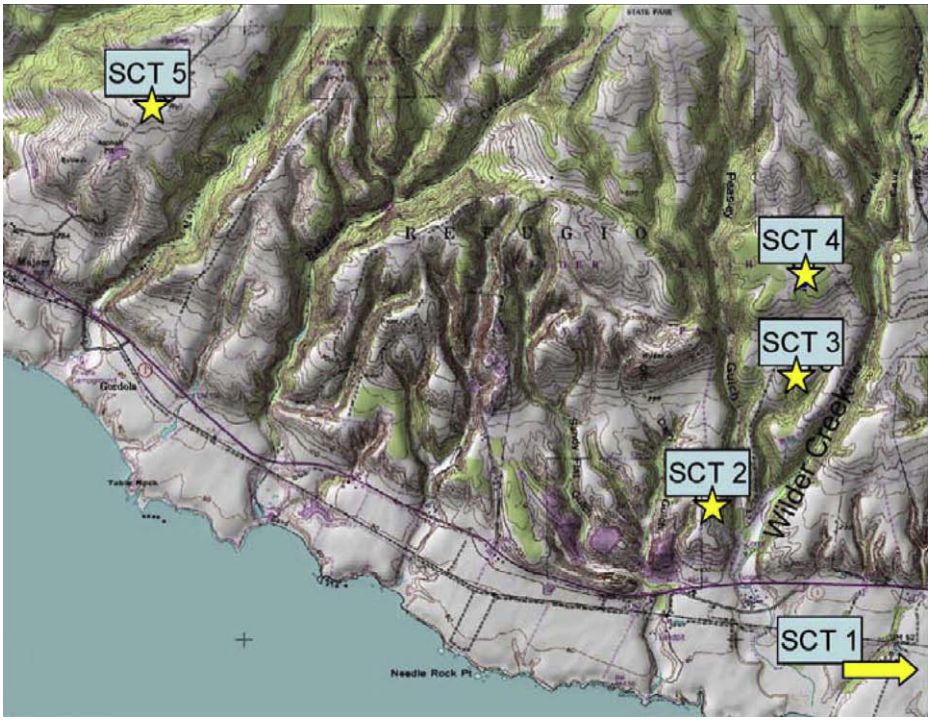

Fig. 1. Location and topography of the Santa Cruz field sites. Location of the SCT 1 site is approximately 5 km east of map area). Site coordinates listed in Appendix A.

sites used techniques similar to those described by White et al. (1998, 2005. Precipitation was measured between March 2001 and March 2004 in Taylor rain gauges. Precipitation compositions were determined from samples collected over one-to-two-week intervals during the rainy seasons using 30 cm diameter plastic funnels covered with plastic mesh and connected to one liter plastic collection bottles. Collection sites were situated in open spaces with minimum through-fall inputs from vegetation.

Water contents were measured gravimetrically on augered soil samples collected at each site on weekly-to-monthly intervals between 2001 and 2004. Soil sample weights were recorded before and after heating to 80 °C for 24 h in the laboratory. Pore water tensions were periodically read from analog ceramic-tipped field tensiometers. During the driest summer months, samplers at depths <1 m commonly exceeded air-entry tensions, precluding tension measurements.

Pore waters from unsaturated soils were collected from nested porous-cup suction water samplers (5 cm dia.) installed in hand-augered holes at depths ranging from 0.15 to 15.2 m. The samplers were evacuated to approximately 80 cbars vacuum and pore waters collected at weekly to monthly intervals from March 2001 to June 2005. Dry conditions and associated low water tensions at depths <1 m precluded water sampling over most of the summer when solute fluxes are thought to be negligible. Water samples were also collected from piezometers completed into the permanent ground water underlying the terraces (except at SCT 2) and from shallow, seasonally-perched ground water at depths of about 1 m.

Pore waters from the suction samplers were filtered (0.1 μm), after determining pH and alkalinity in the laboratory and the chemical compositions were analyzed using ion chromatography (anions) and ICP-mass spectroscopy (cations and Si). $^{87}Sr/^{86}Sr$ ratios were determined by thermal ionization mass spectrometry as described by Bullen et al. (1997). Exchangeable cations were determined using acetate extractions (Amacher et al., 1990). Surface areas were determined by BET/nitrogen sorption and sorption by polyvinylpyrrolidone (Blum and Eberl, 2004).

Gas samplers, consisting of nested 3.2 mm stainless steel tubes, were completed in down-hole sand-packed intervals separated with bentonite plugs. Soil gas samples were collected with plastic syringes and were analyzed in the laboratory within 24 h for CO_2 and O_2 by gas chromatography using the methods of White et al. (2005). During the winter, many of the shallow gas samplers became flooded with perched ground water and did not yield gas samples. Detailed analyses of the terrace mineralogy, elemental compositions and bulk densities are described in White et al. (2008).

3. RESULTS

3.1. Precipitation inputs

The Mediterranean climate produces highly seasonal precipitation at Santa Cruz with significant rainfall between November and May and essentially no rainfall from June to October (Fig. 2a). During the dry season, moisture inputs to the terraces are principally from coastal fog. In California coastal grasslands, similar to those at the Santa Cruz sites, Corbin et al. (2005) found that fog contributed up to 66% of moisture used by non-annual plants during the summer months.

Rainfall exhibits a significant orographic effect, with SCT 1, approximately 6 m above mean sea level (msl), receiving slightly more than half the precipitation of SCT 4 (159 msl) (Table 1 and Fig. 2a). This trend of increasing precipitation does not extend to the highest elevation SCT 5 site (189 msl), which is located more than a kilometer closer to the coastline than SCT 4 (Fig. 1 and Table 1). Discussion of regional precipitation patterns and the orographic effects of the Santa Cruz Mountains are contained in Ralph et al. (2003).

The precipitation data also exhibit significant yearly differences, with 30% more rain falling during the 2001–2002 wet season compared to the 2003–2004 wet season (Fig. 2b). However, the relative differences in precipitation remain consistent between sites for all the years. Average annual rainfall measured at the SCT 1 site during the study period (390 mm, 2001–2004) was higher than a longer-term record measured in the city of Santa Cruz at approximately the same elevation (309 mm between 1948 and 2006, U.S. National Oceanic and Atmospheric Agency database).

The relative proportions of solutes in annual volume-weighted precipitation (Table 1 and Fig. 2c) correlate with those of seawater, i.e., $Cl > Na > Mg \geqslant SO_4 > Ca > K$, implying a dominant marine input. Seawater inputs in coastal environments occur both as wet and dry aerosols, produced primarily by the bursting of air bubbles particularly during wind-intensive winter storms events (Gong et al., 1997). The precipitation collectors were not monitored between May and October of each year and therefore dry deposition is unaccounted for during these periods. The major solutes in rainfall, Cl, Na and Mg, decrease with increasing distance from the coast (Table 1 and Fig. 2c). Such decreases, observed elsewhere along the Pacific Coast (Rossnecht et al., 1973), have been described by exponential decay functions (Gustafsson and Franzen, 2000). The solute fluxes from rain onto the terrace surfaces (mol m^{-2} yr^{-1}) were determined by multiplying volume-averaged solute concentrations, which decrease with elevation and distance from the coast, by the annual precipitation, which generally increases with elevation and distance. The net effect is that precipitation fluxes of the major solutes Na, Mg and Cl are similar across all the terraces (Table 1 and Fig. 2d). The concentrations of other major components, including Ca, K and SO_4, are more variable and reflect additional atmospheric inputs as will be discussed in a subsequent paper.

3.2. Regolith hydrology

The flow paths and rates of water movement through the terrace regoliths are critical to understanding the evolution of solutes and contemporary rates of chemical weathering. Conceptualized water flow is shown in Fig. 3a with details discussed in the following sections.

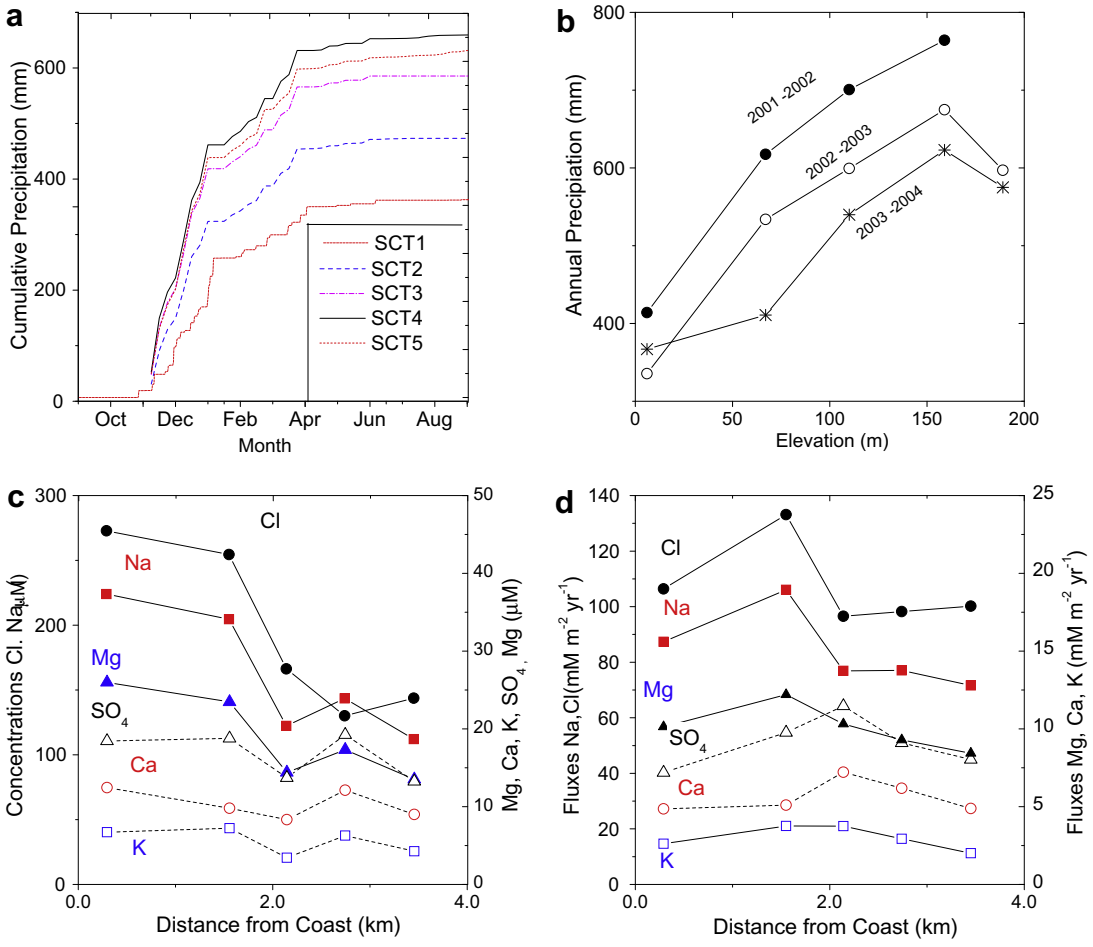

Fig. 2. Precipitation at the Santa Cruz sites. (a) Cumulative rainfall on the individual terraces between Fall of 2002 and Spring of 2003. (b) Annual rainfall vs. terrace elevation for consecutive water years (2001–2003). (c) Volume-weighted rainfall compositions versus distance from the coast. (d) Average annual elemental fluxes vs. distance from the coast.

3.2.1. Soil moisture

Moisture contents for SCT 3 are plotted as functions of depth in Fig. 3b with additional time-dependent data contoured for SCT 1, 2, and 5 in Fig. 4. The seasonality of precipitation and evapotranspiration result in strong variations in soil moisture above the relatively shallow clay-rich argillic horizons (<0.5 m). These horizons are characterized in Fig. 4 by increasing abundances and thicknesses of clay in terraces of increasing age. They are produced from the weathering of primary silicates (principally feldspar) and detrital smectite to form kaolinite (White et al., 2008) Processes leading to their formation is described in detail in a companion paper (Maher et al., 2009).

During the winter months (January to March), shallow moisture contents commonly exceed 20 wt%, indicating saturated or near-saturated conditions in and above the argillic horizon (Fig. 3c). Pore waters saturation is determined from porosity and gravimetric water data. In all but the youngest SCT 1 terrace, saturated conditions are reflected by perched ground water observed in arrays of shallow piezometers (Fig. 3a).

Perched ground waters disappear by May of each year. During the subsequent dry summer months, shallow moisture contents become <2 wt% and the soil saturation diminishes to <5% at shallow depths (Figs. 3 and 4). These depths also correspond to the rooting zones of the predominantly annual grassland vegetation and are subjected to high evapotranspiration rates. ET ranges between 65% and 80% of the total precipitation (Table 1). After dieback in the summer, additional water is lost by direct evaporation and through transpiration by a lower density of perennial grasses and forbes.

Soils beneath the argillic horizons (>2 m) remain generally unsaturated throughout the year (Fig. 3c.) These horizons exhibit more consistent moisture contents that are intermediate between the seasonal wet and dry extremes in the shallow soils (Fig. 4). This hydrologic attenuation results from the relatively low permeability of the overlying argillic horizons. Permanent ground water, as opposed to seasonal perched ground water, was encountered near the maximum sampling depths in each of the terraces (except at SCT 2). Ground waters in SCT 1 and SCT 5 occur above the terrace contacts with the relatively impermeable Santa Cruz Mudstone and, in SCT 3, near the contact with the Ben Lomond Granite. Seasonal variations in water levels, combined with capillary fringe effects, are responsible for

Table 1
Precipitation at the Santa Cruz Terraces.

Sampling interval	SCT1 1/03-4/04	SCT2 9/01-3/04	SCT3 11/00-3/04	SCT4 11/00-4/04	SCT5 1/02-4/04
Elevation (m)	6	67	110	159	189
Distance (km)[a]	0.29	1.55	2.74	3.45	2.14
Annual Precip. (mm)	390	520	596	687	586
ET (%)	80	66	72	65	74
Concentration[b] *(μm)*					
Na	224	204	129	112	122
Mg	26.0	23.5	17.3	13.5	14.4
K	6.72	7.23	6.29	4.26	3.43
Ca	12.45	9.80	12.11	9.00	8.33
Rb	0.0016	0.0019	0.0033	0.0013	0.0049
Sr	0.065	0.055	0.051	0.038	0.043
Cl	273	256	162	143	171
NO_3	8.12	8.72	12.70	6.68	8.28
SO_4	18.44	18.79	19.25	13.24	13.71
$^{87}Sr/^{86}Sr$	0.70910	0.70907	0.70916	0.70911	0.70942
Flux[b] *(mmol/m²)*					
Na	87.4	106.1	76.9	77.0	71.6
Mg	10.13	12.20	10.32	9.29	8.43
K	2.62	3.76	3.75	2.93	2.01
Ca	4.86	5.10	7.22	6.19	4.88
Rb	0.0006	0.0010	0.0019	0.0009	0.0029
Sr	0.025	0.029	0.030	0.026	0.025
Cl	106.4	133.1	96.6	98.2	100.2
NO_3	3.32	4.53	7.57	4.59	4.85
SO_4	7.19	9.77	11.47	9.10	8.03

[a] Minimum distance from coast.
[B] Concentrations and fluxes are volume-weighted averages.

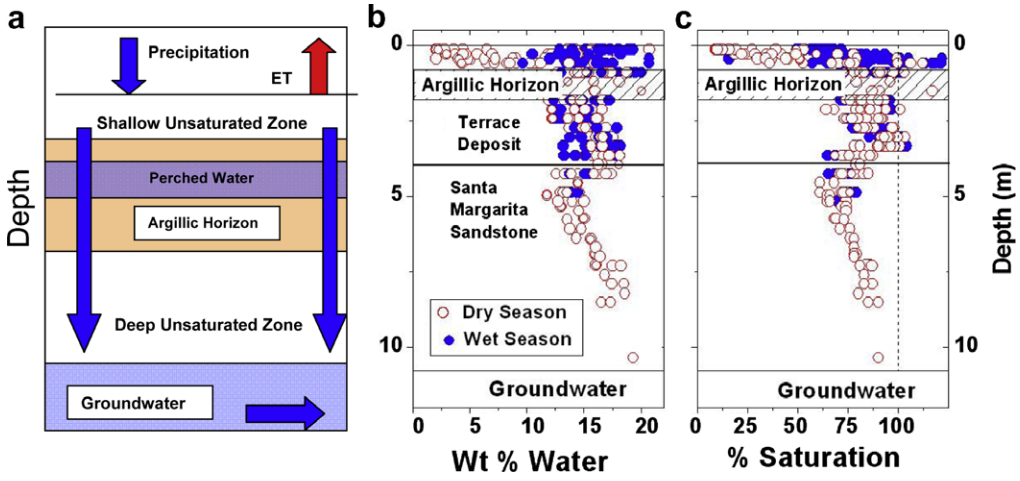

Fig. 3. Hydrologic characteristics of the Santa Cruz Terraces. (a) Schematic showing major hydrologic units and pathways (depth and flow vectors are not to scale). (b) Gravimetric water contents in SCT 3 terrace as measured during the wet (November to May) and dry seasons (June to October). (c) Extent of pore waters saturation during wet and dry seasons calculated from hydraulic parameters contained in Appendix A and from White et al. (2008). Also shown in (b) and (c) are the approximate positions of the argillic horizons and the maximum ground water elevations.

increasing moisture in the unsaturated zones directly above the ground water (Fig. 3b and Fig. 4).

No permanent ground water was encountered in SCT 2, even though it was the deepest profile sampled (>15 m). The significant increase in moisture in basal terrace sediments overlying the contact with Santa Margarita Sandstone (approximately 4 m in Fig. 4) corresponds to a zone of high amounts of detrital smectite (White et al., 2008). The unconsolidated clean coarse sands in the underlying Santa Margarita Sandstone produce a capillary barrier to

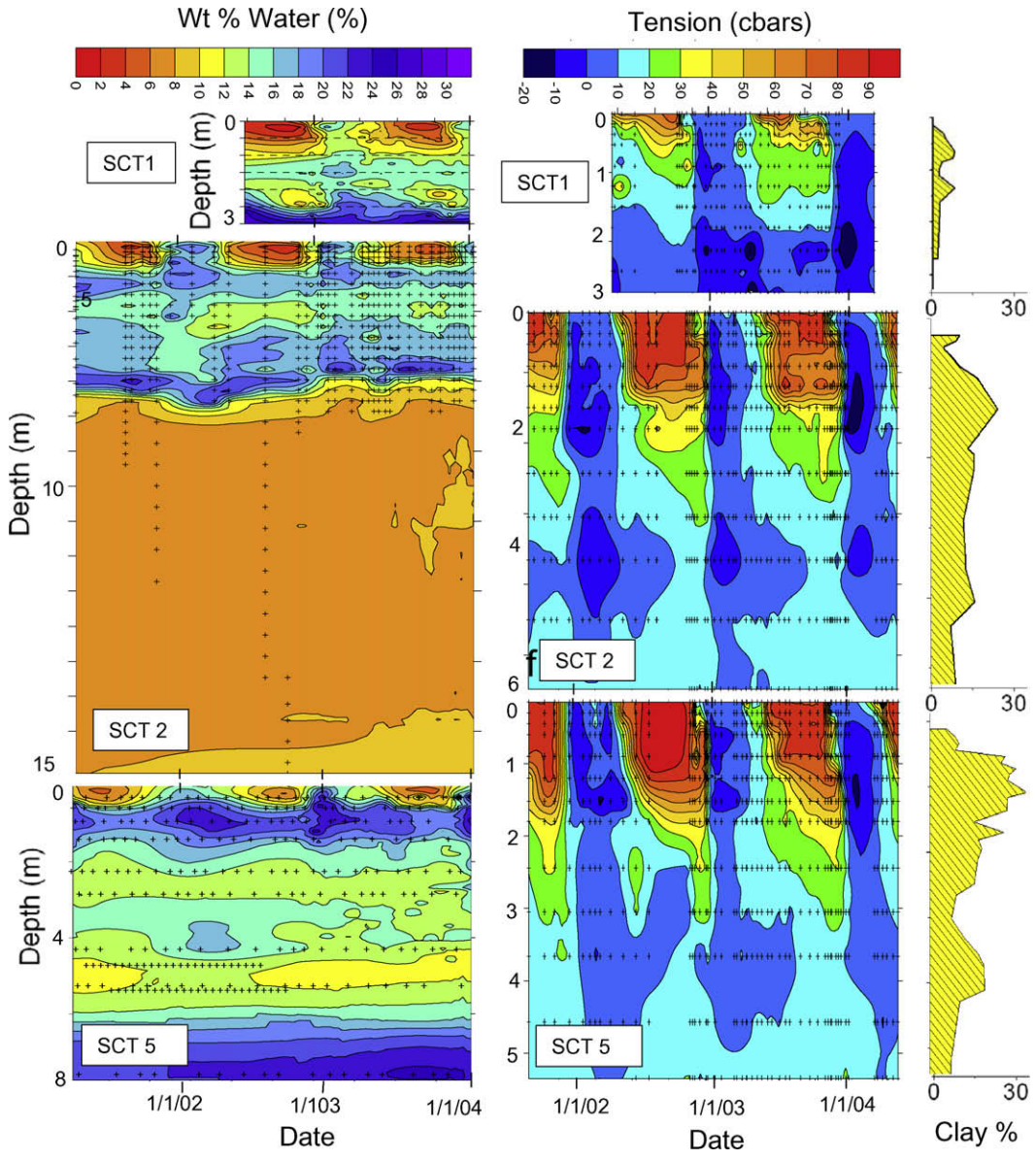

Fig. 4. Contours of soil moisture and tension in the SCT 1, 2 and 5 terraces between June, 2001 and June, 2004. Symbols (+) correspond to individual samples. Also plotted to scale with soil water tensions are kaolinite contents in each terrace. Maximum clay concentrations correspond to the argillic horizon.

downward water movement, producing drier conditions (<8 wt%) that extend to the maximum sampling depth of >15 m.

3.2.2. Soil water tension

Soil water tensions reflect seasonal moisture dynamics and physical soil properties. During the summer months, tensions in the shallow soils become strongly positive, commonly exceeding the air entry values of the ceramic cup tensiometers (~90 cbars). Actual soil water tensions during these periods probably exceed 15 bars vacuum, the approximate wilting potential of the grasses during summer dieback. High tensions at shallow depths during the summer indicate the potential for upward movement of water from moister deeper soil horizons. However, the exponential decreases in hydraulic conductivities as functions of increasing under-saturation make such movement extremely slow (Stonestrom et al., 1998). As indicated by the schematic in Fig. 3a, flow in the deep unsaturated zone is assumed to occur principally as vertical percolation.

While soil water tension is related to soil moisture, it is also dependent on the changing physical properties of the soil as shown by the close correlations with clay content (Fig. 4). SCT 1 is composed of relatively unweathered beach sand, reflective of the original protolith. Such sands, having low surface areas and relatively narrow ranges of pore-size distributions, produce large seasonal changes in moisture content over relatively small changes in tension (Fig. 4). In contrast, in SCT 2 and SCT 5, the higher capillarity of the clays account for larger seasonal variations in

tension, even though the corresponding changes in soil moisture are less than at SCT 1.

While both soil moisture and tension exhibit strong seasonal trends, their spatial patterns diverge with soil age. Seasonal soil moisture variations become confined to progressively shallower depths with increasing soil age whereas seasonal tension variations extend to greater depths. Unlike moisture content, tension varies continuously with depth. For example, while moisture content is discontinuous across the contact between the clay-rich terrace deposit and the underlying sand-rich Santa Margarita Sandstone in SCT 2, tensions vary smoothly. Tensions at depth are essentially constant, reflecting gravity-driven downward flow (Fig. 4).

3.3. Solute chemistry

Representative chemical compositions of precipitation, soil pore waters and permanent and perched ground waters are tabulated in Appendix. Discussion of surface water compositions associated with streams draining the Santa Cruz terraces will be discussed elsewhere. The predominance of solute cations generally decrease in the order $Na > Mg > Ca > K > Sr$. Together with Si, the distributions of these cations, and their relationships to chemical weathering are the principal topics of this paper. Anion concentrations generally decrease in the order $Cl > NO_3 > HCO_3 > SO_4$ (Appendix A). Of these anions, only Cl distributions will be discussed here in terms of defining hydrologic and solute fluxes. The remaining major anions are involved in biologic processes and will be described in detail in a subsequent paper.

3.3.1. Solute Cl compositions

The dominance of Cl as an anion in pore waters is expected for a coastal environment (Table 1). Chloride in the shallow pore waters exhibits wide seasonal variability, ranging from overlapping that of precipitation to values more than an order of magnitude more concentrated (Appendix A and Fig. 5). Seasonal distributions are skewed to lower concentrations than those that actually occur in the shallow soils because, during the driest summer months,

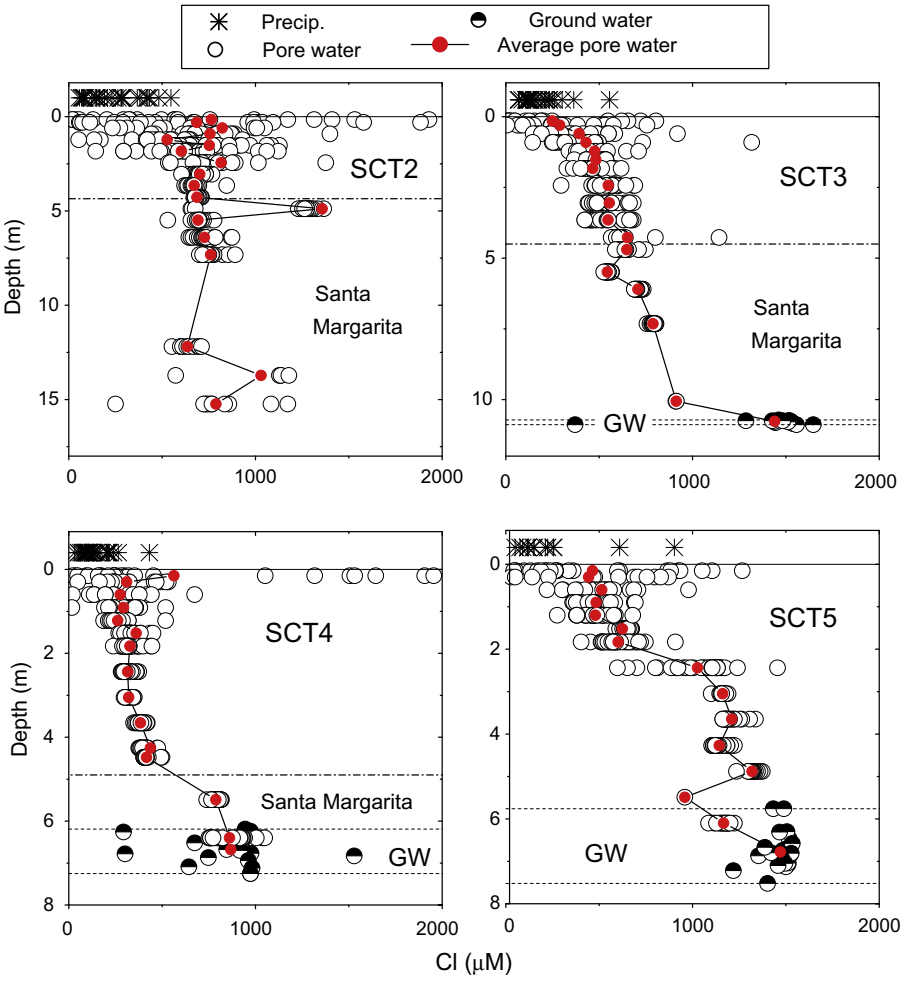

Fig. 5. Chloride in precipitation, pore waters and ground waters. Upper horizontal lines represent the contacts between the terrace sediments and the underlying Santa Margarita Sandstone (not present in SCT 5). Pairs of lower horizontal lines denote maximum and minimum ground water elevations (not present in SCT 2).

shallow samples were unavailable. Chloride is not derived from chemical weathering, and the large variations primarily reflect the seasonality of precipitation and evapotranspiration. In addition, minor amounts of Cl may be cycled in the shallow soil horizons as chlorinated organic compounds and taken up during microbial processes (Bastviken et al., 2007).

Chloride exhibits much less seasonal variability and no strong dependence with depth in the lower terrace deposits and underlying Santa Margarita Sandstone (Fig. 5). As previously indicated, these soils also exhibit damped seasonal moisture fluctuations (Fig. 4). The exception is SCT 5, which exhibits marked Cl increases near the base of the argillic horizon. Chloride is generally higher in the permanent ground waters and in the unsaturated soils immediately above this ground water.

Chloride distributions provide an estimate of ET and, therefore, the average water flow at depth through the terraces. Assuming vertical movement, the hydraulic flux q_h (m s^{-1}) is equal to the net difference between the annual precipitation and ET fluxes

$$q_h = q_{precip} - q_{ET} = q_{precip}\left(\frac{c_{Cl,precip}}{c_{Cl,solute}}\right) \quad (1)$$

This flux, in turn, is equal to the product of the precipitation and the concentration ratio of Cl in volume-weighted annual precipitation $c_{Cl,precip}$ (Table 1) divided by that of average pore waters $c_{Cl,solute}$, which is derived from of samples collected below the depth of seasonal moisture fluctuations but above the influence of the underlying ground water (Table 2). The calculated pore waters fluxes ranged between $q_h = 0.062$ and 0.22 m yr^{-1}.

The macroscopic rate of water movement downward through the terraces is the advective velocity v (m s^{-1})

$$v = \frac{q_h}{\phi\Gamma} = \frac{q_h}{\theta} \quad (2)$$

where φ is the soil porosity (m^3 m^{-3}) and Γ is the pore waters saturation (m^3 m^{-3}) averaged for each terrace below 1 m (Fig. 3 and Appendix A). Values for v are contained in Table 2.

The volumetric water content θ (m^3 m^{-3}) is calculated from the gravimetric water content F_w (Figs. 3 and 4 and Appendix A) as follows

$$\theta = F_w \cdot (\rho_{bulk}/\rho_{water}) \quad (3)$$

where ρ_{bulk}/ρ_{water} is the ratio of soil to water bulk densities.

Dividing the advective velocities calculated from Eq. (2) (0.20 and 0.71 m yr^{-1} in Table 2) by the total terrace depth thicknesses z (Appendix A) results in the average residence time that the given volume of pore waters resides in a terrace profile, which ranges from 10 to 24 yrs (Table 2). Estimates of the hydrologic fluxes are, therefore, dependent on decadal scale rainfall patterns. While the rainfall measured during the 3 yr study period is generally consistent with long term records, significant annual differences have occurred in the recent past. Most notably was the California drought years of 1988–1992 with less than half the long-term average rainfall. These conditions presumably decreased the advective velocities and increased average fluid residence times.

3.3.2. Solute Na distributions

Sodium is the dominant cation in soil pore waters and ground waters (Appendix A). While precipitation provides significant solute inputs due to the close proximity to the ocean (Table 1), additional Na is contributed from mineral weathering, principally from plagioclase (White et al., 2008). Sodium is not subsequently incorporated into or strongly sorbed onto secondary clay minerals (Appendix B), nor is it a major plant nutrient in the grassland vegetation (Table 3). A much more extensive discussion of plant nutrient cycling will be presented in a future paper.

Pore water Na at shallow depths (<1 m) ranged from values comparable to precipitation to higher concentrations reflecting extensive ET (Fig. 6). Solute Na, like Cl, undoubtedly becomes even more concentrated during the driest summer months when shallow pore water sampling becomes impossible. Average measured Na concentrations (shown as lines connecting open circles in Fig. 6) generally increase with increasing sampling depth. In the SCT 2 and

Table 3
Average concentration (wt%) of selected mineral nutrients in grasses on the Santa Cruz Terraces[1].

	K	Ca	Mg	Na	Si
SCT 1	1.13	0.39	0.11	0.09	1.03
SCT 2	0.67	0.46	0.10	0.07	0.83
SCT 3	0.83	0.39	0.11	0.10	0.62
SCT 4	1.00	0.35	0.13	0.11	0.53
SCT 5	0.69	0.57	0.11	0.05	1.10

[1] Average of of above-ground 1 m^2 plots collected over the 2004 growing season.

Table 2
Precipitation and pore water fluxes (m yr^{-1}), Cl concentrations (μM) and hydrologic parameters.

Terrace	Precip. Cl (μM)	Deep pore water Cl (μM)	Precip. Flux, q_{precip} (Eq. (1))	Pore water flux from Cl, q_h (Eq. (1))	Long-term pore water flux, q_h White et al. (2008)	Average porosity[a] Φ (%)	Average saturation[a] Γ (%)	Advective flux, v (Eq. (2)) (m yr^{-1})	Fluid residence time (yr)
SCT 1	273	1623	0.37	0.062	0.025	0.37	0.86	0.198	9.7
SCT 2	256	768	0.52	0.173	0.150	0.46	0.53	0.705	21.6
SCT 3	162	583	0.61	0.170	0.070	0.43	0.83	0.481	22.6
SCT 4	143	452	0.69	0.218	0.095	0.46	0.83	0.569	12.1
SCT 5	171	1136	0.59	0.088	0.058	0.41	0.76	0.283	23.6

[a] Averaged from data in Appendix A.

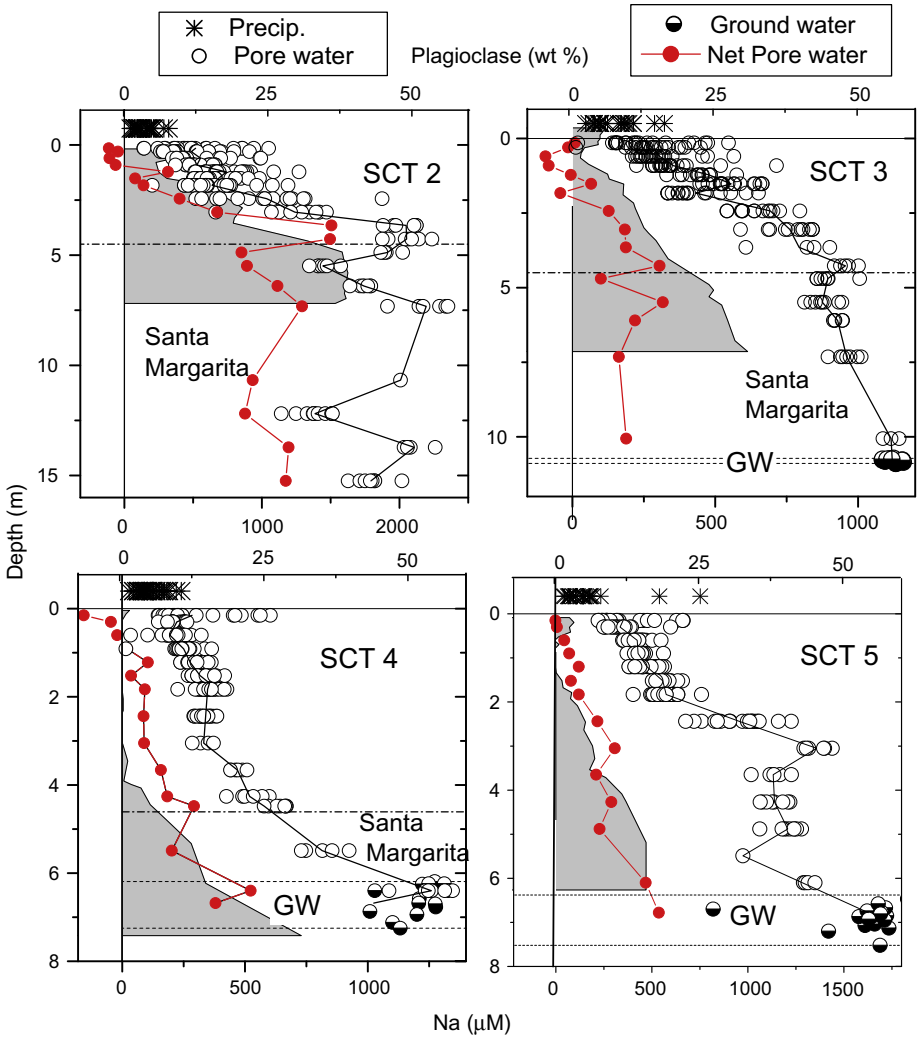

Fig. 6. Sodium in precipitation, pore waters and ground waters. Open circles are measured pore waters concentrations ($c_{Na,solute}$ in Eq. (4)) with lines representing average trends with depth. Solid points are average net Na concentrations at a specific depth, corrected for precipitation ($c_{Na,weather}$ in Eq. (4)). Upper horizontal lines are contacts between the terrace sediments and the Santa Margarita Sandstone (not present in SCT 5). Pairs of lower horizontal lines denote maximum and minimum ground water (GW) elevations (not present in SCT 2). Shaded areas are the plagioclase distribution in wt% (data from White et al., 2008).

SCT 3 terraces, the rates of increase are greater in the terrace sediments than in the underlying Santa Margarita Sandstone (see terrace contact depths in Fig. 6). These differences correlate with significantly lower moisture contents in the coarser-grained Santa Margarita Sandstone (Fig. 6 compared with Fig. 4). Na concentrations in pore waters approach those in ground water directly above the permanent water tables (ground water not reached in SCT 2).

The net Na concentration produced from weathering $c_{Na,weather}$ is the difference between the measured concentration $c_{Na,solute}$, and that contributed by precipitation $c_{Na,precip}$ after correction for ET. Evapotranspiration is defined by the ratio of pore water $c_{Cl,solute}$ to precipitation $c_{C,precip}$ (see Eq. (1))

$$c_{Na,weather} = c_{Na,solute} - c_{Na,precip}\left[\frac{c_{Cl,solute}}{c_{Cl,precip.}}\right] \quad (4)$$

As expected for a coastal environment, the net Na produced from weathering is significantly less than the measured pore water Na concentration as shown by the shifts between the respective Na averages (lines connecting open circles compared to those connecting closed circles in Fig. 6). The extent of this correction is considered a minimum due to a lack of available dry deposition inputs during the summer months.

Net solute Na concentrations are essentially zero in soils near the terrace surfaces, which contain relatively low residual plagioclase (shaded areas in Fig. 6). Both net solute Na and residual plagioclase increase with depth in the deeper terrace deposits. However, in the younger SCT 2 and SCT 3 profiles, these rate of increase do not extend across the contact with the underlying Santa Margarita Sandstone suggesting that plagioclase weathering are much slower in these drier sediments (Fig. 4).

3.3.3. Solute Ca and Sr distributions

Compositions of fresh plagioclase in the Santa Cruz terraces range between An_{25} and An_{33}, with a Sr mol fraction of 0.1–0.2. Weathering of plagioclase is reflected in declining bulk-soil Na, Ca and Sr with decreasing terrace depth and increasing terrace age (White et al., 2008). While these weathering trends are extended to solute Na (Fig. 6), they are not reflected in solute Ca and Sr distributions (Fig. 7).

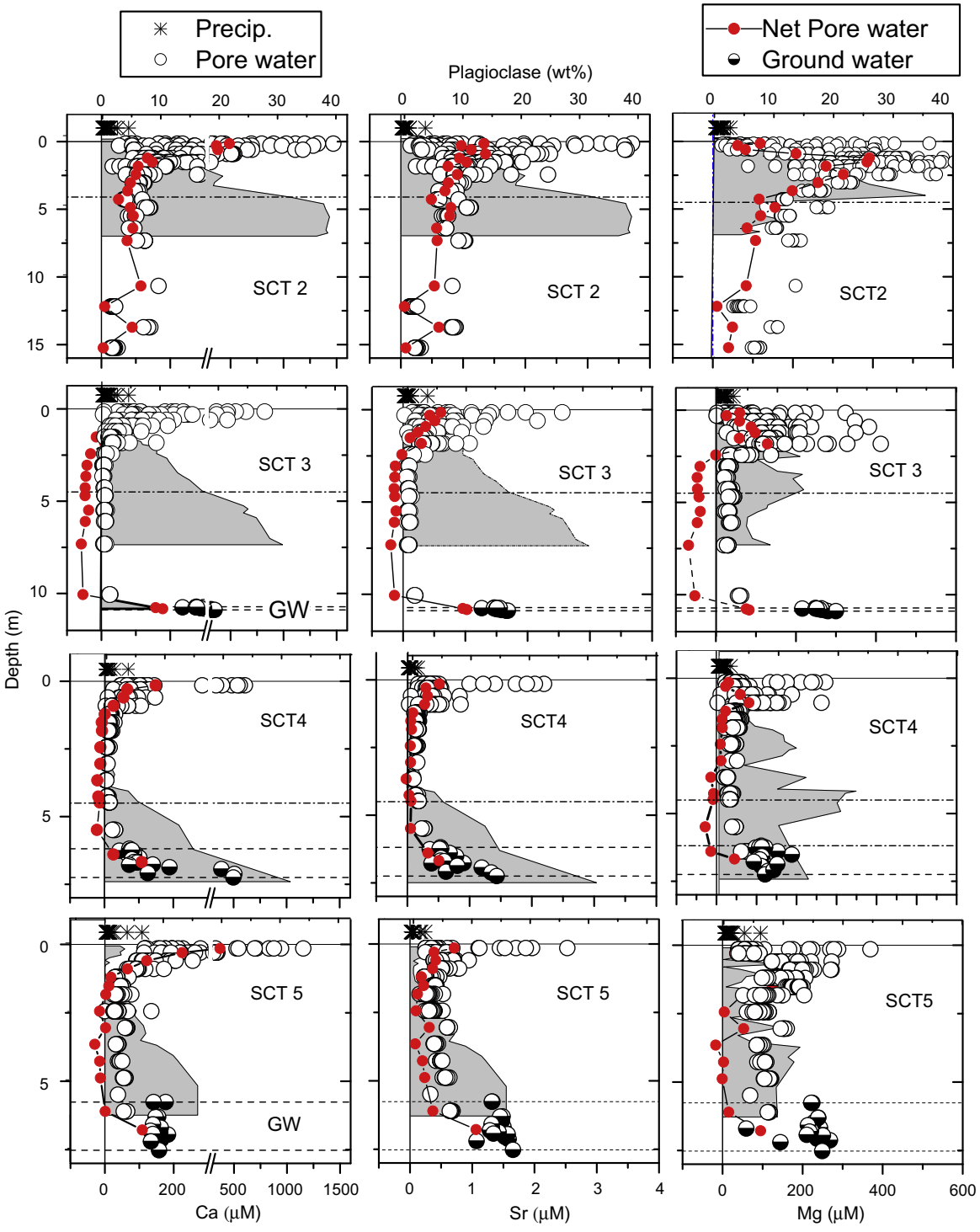

Fig. 7. Calcium, Sr and Mg in precipitation, pore waters and ground waters (note break in Ca concentration axes). Open circles are measured pore waters concentrations. Lines connecting solid points are average concentrations corrected for precipitation. Upper horizontal lines are contacts between the terrace sediments and the Santa Margarita Sandstone (not present in SCT 5). Pairs of lower horizontal lines denote maximum and minimum ground water (GW) elevations (not present in SCT 2). Shaded areas in the Ca and Sr plots correspond to plagioclase distributions and those in the Mg plots correspond to smectite distributions (from White et al., 2008).

Calcium and Sr exhibit much larger variations than Na in shallow pore waters due to significant uptake and cycling in the vegetation (Table 3). However, measured Ca and Sr concentrations are low deeper in the soil profiles and show no correlations with increasing amounts of residual plagioclase (Fig. 7).

Net average Cl-corrected solute Ca and Sr concentrations (based on calculations analogous to Eq. (4)) are even lower than the measured concentrations and, at some depths, produce negative values indicating elemental losses relative to the initial inputs from precipitation (solid circles in Fig. 7). These results indicate that processes other than plagioclase weathering are dominating Ca and Sr distributions in the Santa Cruz terrace pore waters.

3.3.4. $^{87}Sr/^{86}Sr$ distributions

$^{87}Sr/^{86}Sr$ ratios are employed to better understand solute Sr, and by analogy Ca distributions described in the preceding section (Fig. 7). Selected analyses of $^{87}Sr/^{86}Sr$ in precipitation, pore waters and acetate-exchangeable extracts are reported in Appendix B and plotted in Fig. 8 as functions of depth in the SCT 2, SCT 3 and SCT 5 terraces. Pore water $^{87}Sr/^{86}Sr$ values exhibit consistent declines with terrace depth which are contrasted to the lack of vertical trends in solute Sr and Ca (Fig. 7). Solute $^{87}Sr/^{86}Sr$ trends also correlate inversely with increases in solute Na (Fig. 6), suggesting a progressive mixing with depth of relatively radiogenic Sr in precipitation (precipitation = 0.7090–0.7094; seawater = 0.70920), with a less radiogenic Sr derived from plagiolcase.

Strontium distributions are investigated further by considering $^{87}Sr/^{86}Sr$ and Rb/Sr distributions in the granitic source rocks in plutons in the adjacent Santa Cruz Mountains (Kistler and Champion, 2001). Linear regressions through these ratios (Fig. 9) bracket average $^{87}Sr/^{86}Sr$ and Rb/Sr compositions of the deepest unweathered bulk

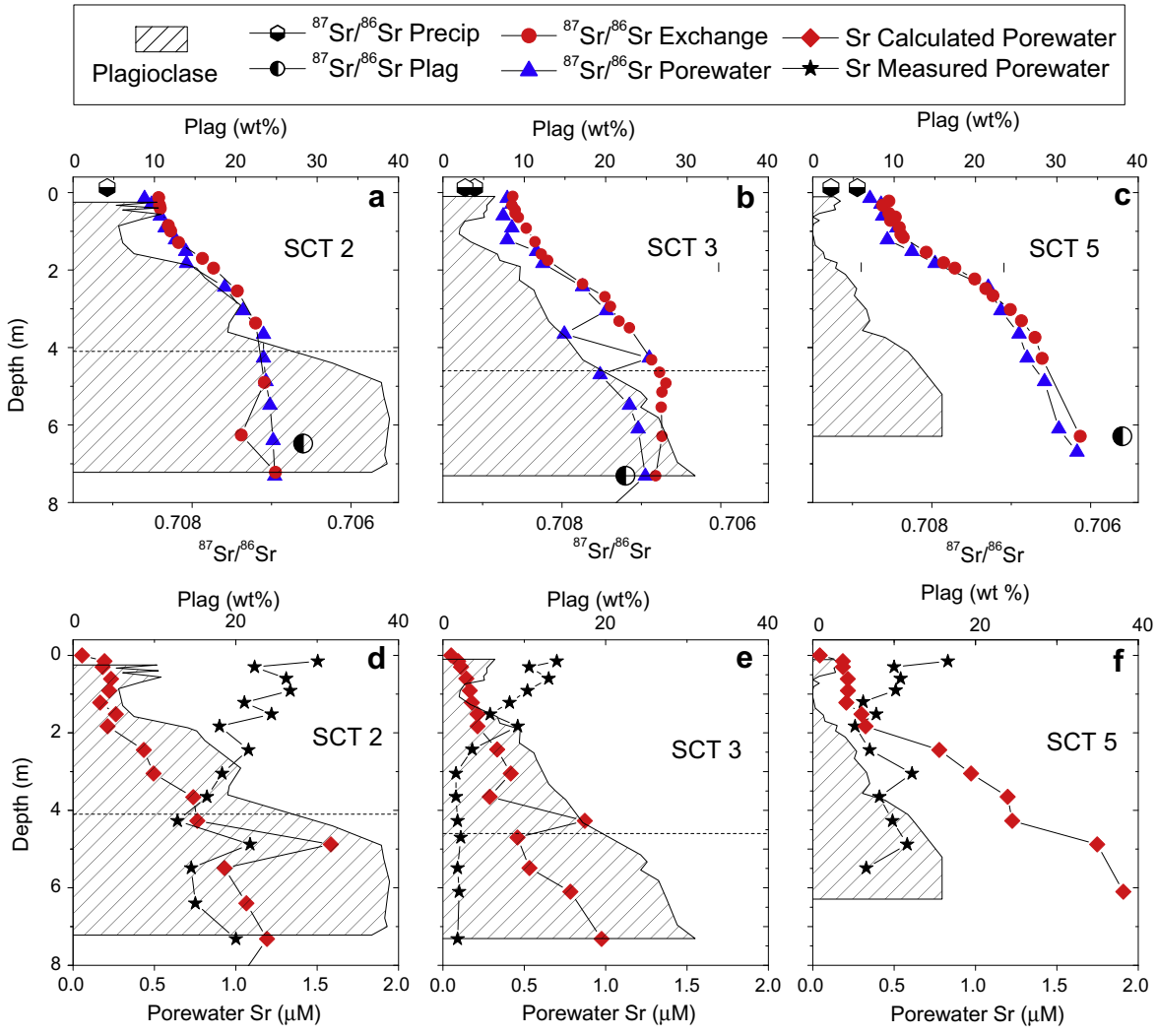

Fig. 8. $^{87}Sr/^{86}Sr$ distribution in precipitation, pore waters and acetate-exchangeable extracts (a–c). Data are contained in Appendix B. Note that $^{87}Sr/^{86}Sr$ axes are reversed relative to common convention for direct comparisons with plagioclase profiles indicated by hatched areas. The isotopic ratios in plagioclase are based on the data shown in Fig. 9. Sr concentrations (Appendix A and Fig. 7) are compared in (d–f) with predicted values based $^{87}Sr/^{86}Sr$ distributions (Eqs. (5) and (6)).

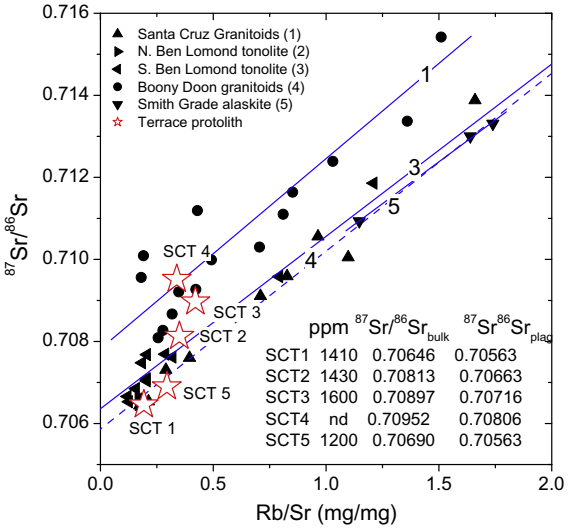

Fig. 9. $^{87}Sr/^{86}Sr$ and Rb/Sr compositions of granitic rocks of the Santa Cruz Mountains (data from Kistler and Champion, 2001) and average compositions for bulk terrace sediments (deepest samples). Plagioclase isotopic ratios are calculated from the intercepts of the linear regressions (Eq. (6)).

terrace sediments. This correlation supports the conclusions of Perg et al. (2003) and White et al. (2008) that the principal sources of terrace sediments are these granitic plutons. Many of the $^{87}Sr/^{86}Sr$ and Rb/Sr ratios of the granitic rocks are significantly higher than those of the terrace protoliths, reflecting the relatively rapid oxidation and weathering of biotite and hornblende (Blum and Erel, 1997; Bullen et al., 1997). A lack of any correlation between $^{87}Sr/^{86}Sr$ and the ages of individual terraces implies that radiogenic Sr was lost during subaerial and/or marine weathering of the sediments prior to terrace deposition.

Plagioclase and K-feldspar are the two residual granite-derived silicates expected to dominate the Rb/Sr and $^{87}Sr/^{86}Sr$ distributions in the terraces (Fig. 9). Significant amounts of detrital smectite are also present in the younger SCT 1 and SCT 2 terraces (Fig. 7c). However, there is a lack of consistent differences in Rb/Sr and $^{87}Sr/^{86}Sr$ in these terraces relative those ratios in the older low-smectite terraces.

Extrapolation of the linear regression through the pluton and bulk soil data to zero Rb/Sr ratios produces the estimated plagioclase $^{87}Sr/^{86}Sr$ values listed in Fig. 9. This technique rests on the fact that Rb concentrations are much lower in plagioclase than in other minerals crystallizing from granitic melts such as K-feldspar and micas.

These extrapolated $^{87}Sr/^{86}Sr$ values (Fig. 9) are significantly less radiogenic than for precipitation (Fig. 8). The deepest pore waters in each of the terraces approach the corresponding calculated plagioclase $^{87}Sr/^{86}Sr$, suggesting that Sr accumulation during pore water percolation becomes progressively dominated by weathering relative to the initial precipitation inputs (Fig. 8).

The expected solute Sr concentrations ($c_{Sr,solute}$) at any depth in the terraces can be approximated by mixtures of Sr contributed from precipitation $Ss_{r,precip}$ and from plagioclase weathering $m_{Sr,plag}$ (mol)

$$c_{Sr,solute} = \frac{m_{Sr,precip} + m_{Sr,plag}}{m_{solute}} \quad (5)$$

where m_{solute} is the pore water mass (kg). Eq. (5) makes the assumption that other minerals, principally K-feldspar, are not contributing significantly to pore water Sr. This is a reasonable first approximation based on lower K-feldspar concentrations in the initial sediments and slower subsequent weathering rates (White et al., 2008).

Sr contributed from plagioclase $m_{Sr,plag}$ is calculated from the isotopic ratios in pore waters, plagioclase and precipitation.

$$m_{Sr,plag} = m_{Sr,precp}\left[\frac{^{87}Sr/^{86}Sr_{solute} - {}^{87}Sr/^{86}Sr_{precip}}{^{87}Sr/^{86}Sr_{plag} - {}^{87}Sr/^{86}Sr_{solute}}\right] \quad (6)$$

Average measured $^{87}Sr/^{86}Sr_{precip}$ values for precipitation are listed in Table 1 and for pore waters in Appendix B.

Pore water Sr concentrations, calculated from Eqs. (5) and (6), exhibit progressive increases with depth that are consistent with cumulative inputs from plagioclase weathering (Fig 8). These predicted Sr increases are in marked contrast with very low measured Sr concentrations in pore waters. The only way to reconcile these differences is to invoke a process that does not fractionate $^{87}Sr/^{86}Sr$ but removes Sr, and by analogy, Ca, from the pore waters at rates as fast as it is contributed by chemical weathering.

3.3.5. Solute Mg distributions

Solute Mg is concentrated at shallow terrace depths (<1 m) but to a lesser degree than Ca (Fig. 7). This occurs despite higher Mg concentrations in precipitation (Table 1). However, Mg is present in lower concentrations than Ca in the grassland biomass, suggesting a smaller impact from biological cycling (Table 3). A correlation exists between bulk soil Mg and detrital smectite deposited in the fine-grained component of the original terrace sediment (White et al., 2008). Thermodynamic calculations suggest that pore waters are substantially undersaturated with respect to smectite which is subjected to continuous weathering (Maher et al., 2009). As a result of weathering, this clay generally decreases in abundance both at shallower depths in individual terraces and in overall abundance in terraces of increasing age (Fig. 7).

As expected from the smectite distributions, solute Mg is generally higher in younger terrace deposits than in the older terraces (Fig. 7). However, solute Mg does not correlate directly with smectite profiles in individual profiles. As shown for SCT 2 (Fig. 7), while smectite increases toward the base of terrace deposit, solute Mg decreases. Analogous to Ca and Sr, measured solute Mg is present at low concentrations deeper the terraces, with Cl-corrected values commonly approaching zero or negative, indicating net losses relative to precipitation.

3.3.6. Solute K distributions

Potassium concentrations in the shallow pore waters are generally in excess of those in precipitation and, at their maximum values, approach those of Na (open circles in 10). Potassium levels are much lower in precipitation than those of Na (Table 1), thus eliminating ET as the sole pro-

cess by which K is concentrated. Potassium is the primary mineral nutrient contained in the grasses (Table 3) and large variations in shallow pore waters, like Ca and Sr, reflect biologic cycling. Solute K concentrations decrease significantly in the argillic horizon, but increase again at depth, reaching concentrations comparable to ground water concentrations (Fig. 10).

Average Cl-corrected K concentrations generally parallel those measured in pore waters (solid circles in Fig. 10). The increase in net solute K near the surface reflects biologic cycling and also parallels the increase in eolian K-feldspar (described by White et al., 2008). Net decreases to low or negative K values in the argillic horizon suggest the possible uptake by clays. Deeper in the terrace deposits, net solute K again increases (except for SCT2) suggesting a weathering input dominated by K-feldspar (Fig. 10).

3.3.7. Solute Si distributions

Dissolved silica is not contained in significant concentrations in precipitation and, unlike cation distributions, is not corrected for precipitation inputs in weathering calculations. Elevated Si in the shallow soils (Fig. 11) reflect the combined effects of ET, cycling by grassland vegetation, which contains relatively high amounts of silica in phytoliths (Table 3) and weathering of eolian-derived silicates. Solute Si decreases within the argillic horizons and then increases in the deeper terrace deposits down to the basal contact with the Santa Margarita Sandstone (not present in SCT 5). Similar to solute Na (Fig. 6), the rate of solute Si increase with depth within the Santa Margarita Sandstone is significantly less than in the terrace deposits and corresponds to decreasing moisture contents (compare Fig. 11 with Figs. 3 and 4).

Maximum solute Si concentrations do not become seasonally limited by amorphous SiO_2 saturation (at about 1500 μM) as observed for pore waters in drier soils (Chadwick et al., 1987; White et al., 2005). Although the spatial patterns of solute Si are consistent with those of plagioclase through the profiles, their relative proportions, unlike for solute Na, are not. Although the amount of residual

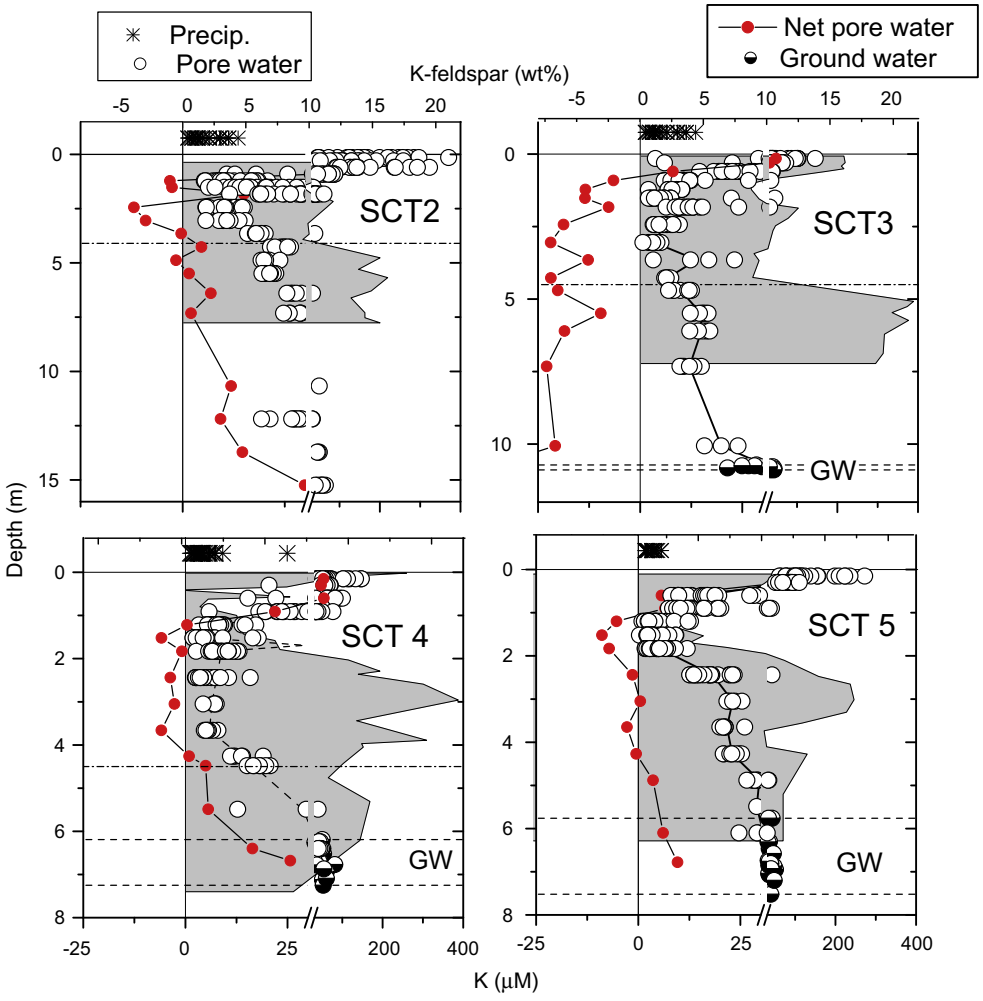

Fig. 10. Potassium in precipitation, pore waters and ground waters (note break in axes). Open circles are measured pore water concentrations. Lines connecting solid points are average concentrations corrected for precipitation. Upper horizontal lines are contacts between the terrace sediments and the Santa Margarita Sandstone (not present in SCT 5). Pairs of lower horizontal lines denote maximum and minimum ground water (GW) elevations (not present in SCT 2). Shaded areas are K-feldspar concentrations (from White et al., 2008).

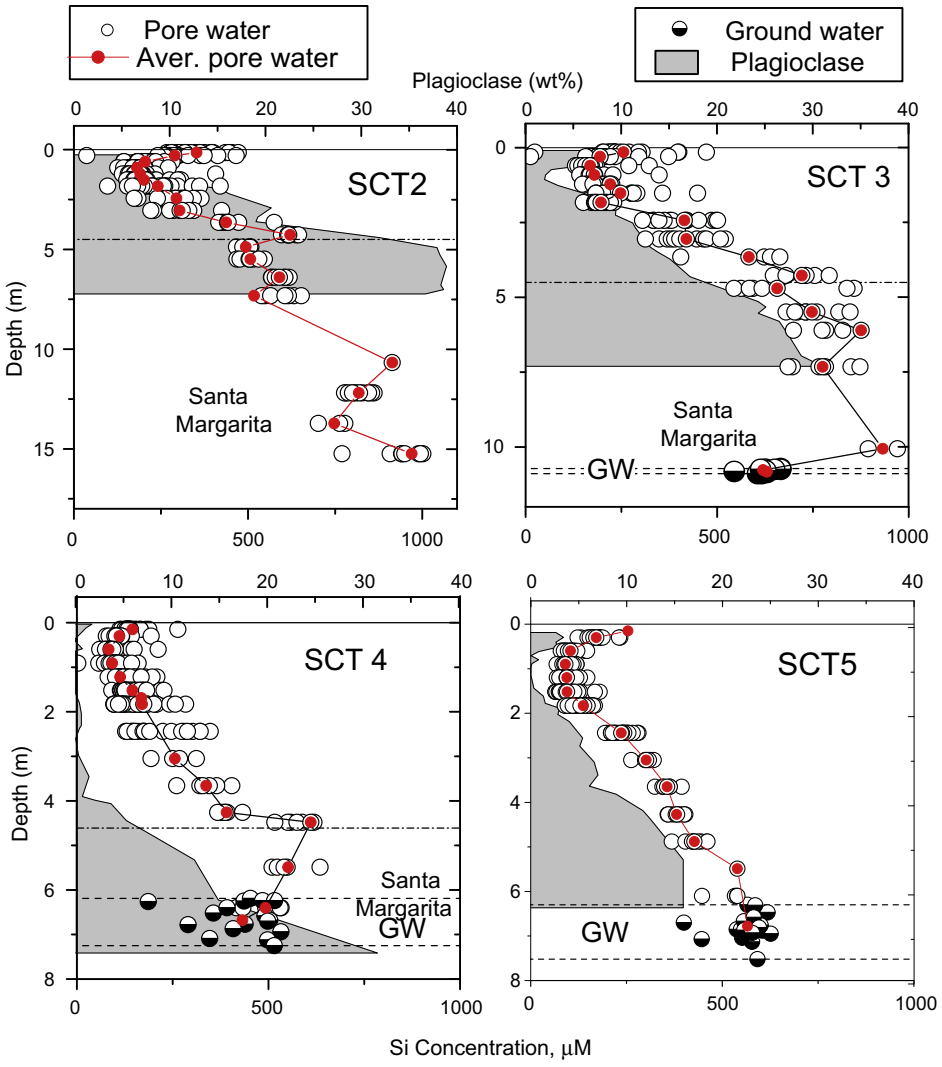

Fig. 11. Silica concentrations in pore waters and ground waters. Open circles are measured concentrations and connected closed circles are average concentrations. Upper horizontal lines are contacts between the terrace sediments and the Santa Margarita Sandstone (not present in SCT 5). Pairs of lower horizontal lines denote maximum and minimum ground water (GW) elevations (not present in SCT 2). Closed data points are the averages of measured pore water concentrations. Shaded areas are plagioclase concentrations (from White et al., 2008).

plagioclase is much higher in the younger terraces than in the older ones at comparable depths, solute Si distributions are similar. This difference reflects the fact that Si is derived from other weatherable silicates, principally K-feldspar and also from smectite which is contained in significant concentrations in the younger terrace deposits. Silica is also incorporated into secondary minerals, principally kaolinite.

3.3.8. *Aluminum and pH distributions*

Hydrogen ion and Al, although present in very low concentrations, are cations that are important in terms of understanding weathering processes. Measured pHs of the suction water samples ranged between about 5.1 and 7.3 (Appendix A) and generally increased with terrace depth. These measured values, reflecting degassing under evacuated conditions in the samplers (White et al., 2005) were corrected by assuming equilibrium between dissolved carbonate species (DIC as alkalinity in Appendix A) and soil gas CO_2 which was independently determined and ranged generally between 0.01 and 0.1 atm. as shown in Fig. 12a (additional data and discussion of soil gases will be presented in a future paper). Calculations by the PHREEQC speciation code (Parkhurst and Appelo, 1999) produced average *in situ* pH values which were consistently lower than the measured pHs (compare pH values in Fig. 12b with those in Appendix A). *In situ* pH decreased across the argillic horizons in the older soils due to the precipitation of Fe-oxyhydroxides and kaolinite and gradually increased again at depth, reflecting silicate hydrolysis reactions that gradually consumed hydrogen ions.

Aluminum commonly complexes with dissolved organic carbon in addition to forming both organic and inorganic colloids (Driscoll et al, 1985; Boudot et al., 1996; Pokrovsky et al., 2005). Such complexation is implied by the close correlation between total Al and dissolved organic matter (DOC) at shallow pore water depths (Figs. 12c and d;

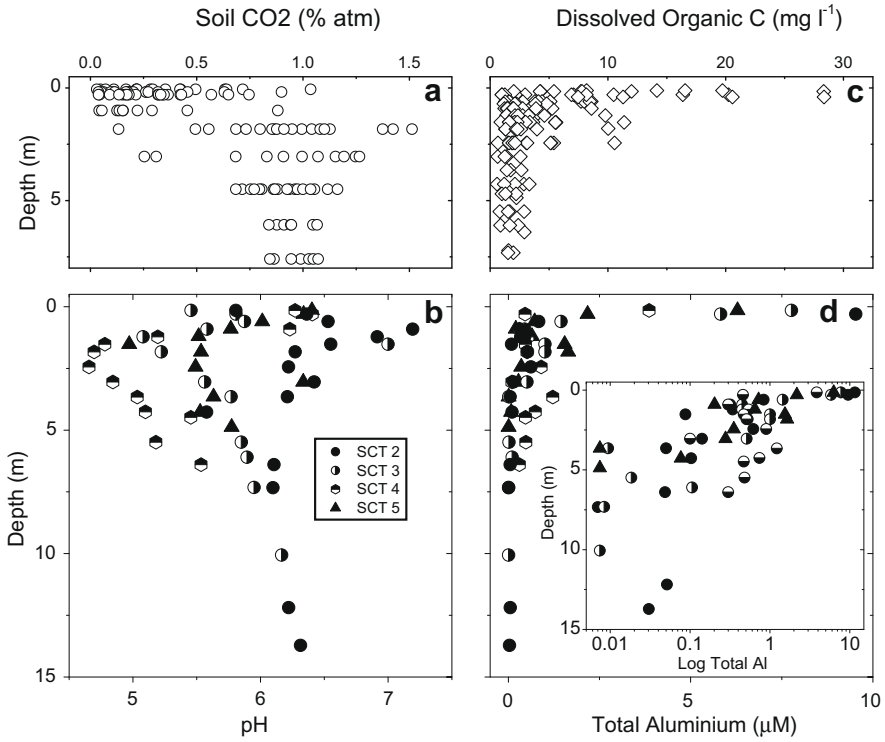

Fig. 12. Correlations between measured soil gas CO_2 and calculated pore pH (a and b) and correlations between dissolved organic carbon and total aluminum (c and d). Aluminum is also plotted on log concentration scale in inset in (d).

additional data and discussion of soil organic carbon will be presented in a future paper). Within the rooting zone of the grassland vegetation (<1 m), high DOC (up to 30 mg l^{-1}) correlates with high total dissolved Al (up to 10 μM). As a consequence of such complexation, the total solute Al at shallow depths is expected to be higher than the activities of inorganic Al species that control mineral saturations. DOC decreases rapidly with increasing depth, reaching concentrations of <1 mg l^{-1}. Corresponding low total Al concentrations of <0.01 μM probably more accurately reflect uncomplexed monomeric Al and inorganic mineral saturation.

3.4. Mineral solubilites and saturation indices

The extent of mineral thermodynamic saturation is important in controlling solute compositions, determining the relative stability of primary and secondary minerals and in influencing kinetic reaction affinities. Mineral saturation, defined as the saturation index (SI), is the log ratio of the ionic activity product in solution (IAP) divided by the mineral solubility constant (K_s). The PHREEQC speciation code (Parkhurst and Appelo, 1999) was employed to calculate SI using mineral K_s values contained in Maher et al. (2009) and corrected to average Santa Cruz soil temperatures (13.5 °C). Considerable uncertainties are associated with mineral-saturation states in weathering environments due to difficulties in measuring field-based solute parameters, as discussed for pH and Al in the preceding section, in addition to uncertainties in specific mineral solubility constants (K_s).

3.4.1. Plagioclase

Multipoint microprobe analyses of a number of plagioclase grains indicate compositions ranging between An_{25} and An_{32} (White et al., 2008) which is consistent for sediments derived from granitic plutons in the Santa Cruz Mountains (also see $^{87}Sr/^{86}Sr$ distributions in Fig. 8). One approach of estimating plagioclase thermodynamic solubilites, at least in the case for more sodic olgioclase and andesine phases commonly associated with granitic rocks, is to equate them to that of the albite end-member (White, 1995; White et al., 2001). The other approach is to approximate the solubility of a plagioclase of a specific An content as a solid–solution between albite and anorthite (Arnórsson and Stefánsson, 1999).

Plagioclase solubility profiles, defined by the end member albite are calculated from the relationship

$$NaAlSi_3O_{8(albite)} + 4H^+ + 4H_2O \rightarrow Na^+ + 3H_4SiO_4 + Al^{3+}$$
$$\log K_{plag} = 3.05(13.5\,^{\circ}C) \quad (7)$$

and are plotted in Fig. 13a. The apparent approach to albite saturation in the shallowest soils is due to the fact that Al concentrations used in equilibrium calculations were not corrected for the important contributions of Al-DOC complexation. (compare Fig. 13a with Figs. 12c and d) The extent of pore water undersaturation at intermediate depths (about 2 m) is dependent on terrace age. Pore waters in the SCT 2 terrace, which has the most residual plagioclase (Fig. 6), are only moderately undersaturated, whereas SCT 4 and SCT 5 terraces, which are most depleted in plagioclase, have pore waters that are the most undersaturated (Fig. 13a).

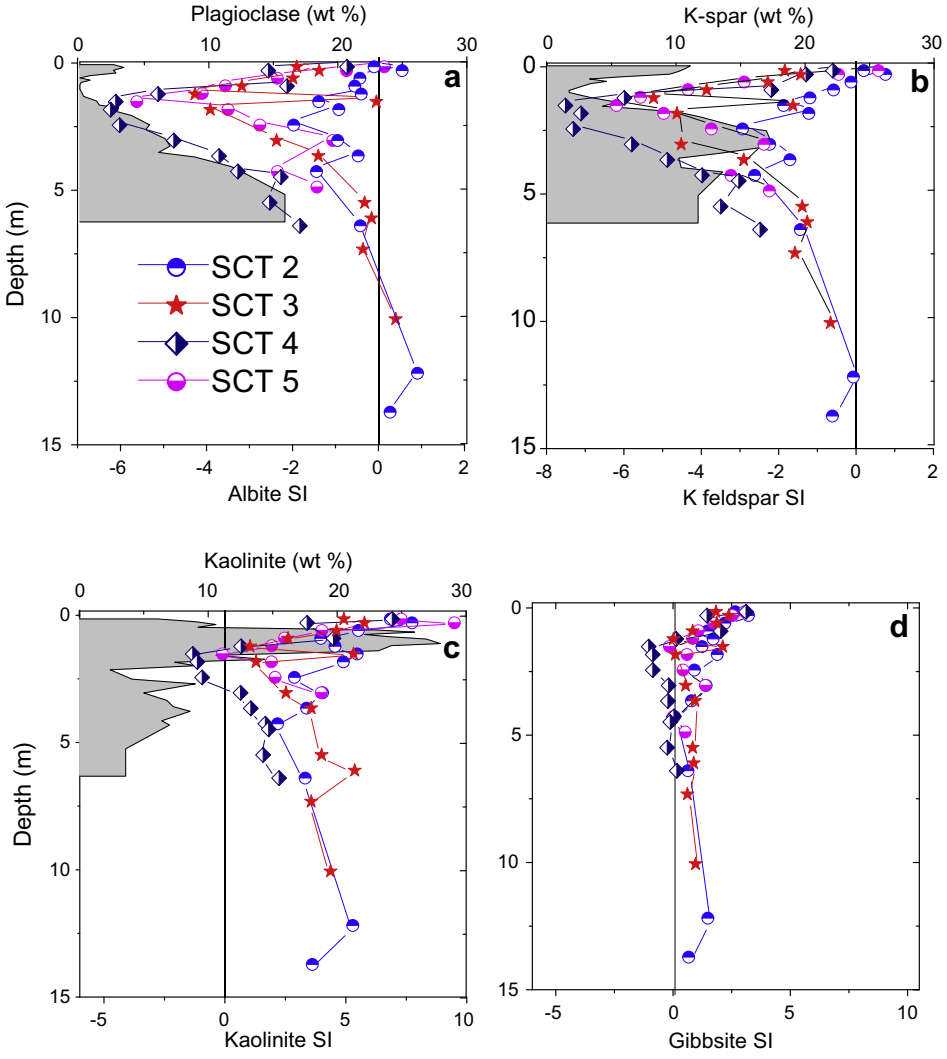

Fig. 13. Saturation indices (SI) for (a) plagioclase (albite) (Eq. (7)) (b) K-feldspar (Eq. (8)). (c) kaolinite (Eq. (9)) and (d) gibbsite (Eq. (10)). Also included in (a–c) are the corresponding mineral distributions for SCT 5 (White et al., 2008).

The extent of plagioclase (albite) undersaturation progressively diminishes at depths below 2 m in all the terraces, reflecting both increasing pore water residence times and plagioclase abundances. At depths in excess of 6 m in the SCT 2 and SCT 3 terraces, pore waters reach or slightly exceed albite saturation (SI $\geqslant$ 0). These depths correspond closely the intervals in which pore water Na no longer increases (Fig. 6) and $^{87}Sr/^{86}Sr$ ratios no longer decrease (Fig. 8a and b), implying the cessation of significant plagioclase weathering inputs. This conclusion is consistent with the observation that amount of plagioclase, as determined by X-ray analyses, remains about constant at these depths. These conditions make a strong argument that pore waters, during vertical infiltration, eventually reach albite thermodynamic saturation at which point further plagioclase weathering ceases. Such thermodynamic saturation is undoubtedly enhanced by the lower moisture contents and, therefore, smaller water/mineral ratios in the Santa Margarita Sandstone (Figs. 6 and 7).

Due to the very large differences in the end member solubilites of albite and anorthite, the solid–solution approach of Arnórsson and Stefánsson, 1999 produces intermediate plagioclase K_s values which are much greater than of the albite end member (Eq. (7)). A K_s for An_{30}, based on such an ideal solid–solution (Maher et al., 2009), produces pore waters that are strongly undersaturated in all the terraces. Such predicted solubility does not reproduce the solute and plagioclase distributions in the soil profiles which imply saturation-limited weathering at depth. A further analysis of the negative implications related to plagioclase solid–solution solubilites is presented by Maher et al. (2009).

The solid–solution approach for estimating plagioclase solubilites requires a homogenous composition. However, detailed reviews (Smith and Brown; 1988; Deer et al., 2001 concluded that plagioclases in the range An_{25} to An_{80} (which includes the Santa Cruz plagioclases) commonly consist of intergrowths of blocks or lamellae with albite-like and anorthite-like structures. Various interpretations of structural reflections invoke the alternation of Ca-rich and Na rich lamellar. These exsolution features develop during the transition of a poorly ordered high temperature phase, comparable to high albite, to more

ordered exsolved phases, more similar to low albite. The transition temperatures are relatively low (400–800 °C) but are readily achieved in slowly cooling granitic plutons.

The scale of these plagioclase lamellae or intergrows, as interpreted by X-ray diffraction patterns and HRTEM images, are extremely small and do not correspond to optical-scale twinning (Olsen, 1974; Kumao et al., 1987). This submicron scale explains the apparent homogeneous composition of the Santa Cruz plagioclases based on resolution of electron microprobe analyses (>10 μm; White et al., 2008). Heterogeneities within these intermediate plagioclases may also explain the role of albite solubility in controlling plagioclase dissolution as evident in the Santa Cruz weathering profiles (Fig. 13a). Until the An-rich component is exposed at or near the surface of weathering plagioclase grain, it remains effectively shielded from reaction until the surrounding albite is dissolved. This process is compatible with the observation that Ca is weathered to only slightly greater depths in the Santa Cruz profiles than is the corresponding Na (see Fig. 9; White et al., 2008).

3.4.2. K-Feldspar

K-feldspar, the other major primary aluminosilicate in the Santa Cruz terraces, has an average composition of Ab_{20} (microprobe analyses; White et al., 2008), a value common for granitic rocks (Deer et al., 2001). K-feldspars exhibit significant perthitic twinning, as documented in thin section, and show preferential weathering of the albitic lamellae at the grain surfaces as seen in SEM images. The relationship between K-feldspar structure, compositions and weathering are extensively discussed by Parsons and Lee (2005).

A parallel argument to that of plagioclase, can be made for K-feldspar, in that its solubility during weathering is approximated by the more insoluble pure orthoclase endmember such that

$$KAlSi_3O_{8(Kspar)} + 4H^+ + 4H_2O \rightarrow K^+ + 3SiO_2 + Al^{3+} + 2H_2O$$
$$\log K_{Kspar} = 1.47(13.5\,^\circ C) \quad (8)$$

The K_s value for K-feldspar (Eq. (8)) is approximately 500 times less than plagioclase (Eq. (7)), a solubility difference used by White et al. (2008) and Maher et al. (2009) to explain, in part, why K-feldspar weathering profiles in Santa Cruz are significantly shallower than those of plagioclase (Fig. 13a and b). The role of differential feldspar solubilites on the long term development of weathering profiles has also been discussed by Nesbitt et al. (1997) and White et al. (2001).

In spite of this solubility difference, K-feldspar saturation indices for pore waters are very similar to that of plagioclase (albite) (Fig. 13a and b). K-feldspar SI values are high near the terrace surfaces, decrease at intermediate depths and, like albite, approach saturation at maximum depths in the SCT 2 and SCT 3 terraces. This similarity in the two feldspar saturation profiles reflect the fact that pore water Na concentrations are 2–3 orders of magnitude greater than K (Figs. 6 and 10 and Appendix A), principally due to high Na inputs from precipitation in the coastal environment (Table 1 and Fig. 2C). In addition, pore K concentrations are very low, reflecting uptake during nutrient cycling by vegetation (Fig. 10). The net result is that the IAPs for albite (Eq. (8)) are significantly greater than those of K-feldspar (Eq. (8)), thus effectively counteracting the intrinsic difference in albite and K-feldspar solubility constants.

Unlike for plagioclase, patterns of pore water K-feldspar saturation with depth do not correlate directly with the distributions of residual K-feldspar, e. g., minimum SI values occur deeper in the terraces than do minimum mineral concentrations. Likewise K-feldspar saturation indices continue to increase at depths below which any consistent increases in residual K-feldspar occur. These contrasts suggest either that K is being contributed at depth by other minerals not restrained by thermodynamic saturation, possibly mica or smectite, or else pore water compositions in the past resulted in different patterns of K feldspar saturation than those observed today.

3.4.3. Kaolinite

The solubility of kaolinite, the dominant secondary mineral in the Santa Cruz terraces, is described by the reaction;

$$Al_2Si_2O_5(OH)_{4(kaolinite)} + 6H^+ \rightarrow 2Al^{3+} + 2H_4SiO_4 + 2H_2O$$
$$\log K_{kaolinite} = 8.49(13.5\,^\circ C) \quad (9)$$

As commonly observed in other weathering environments (White, 1995; White et al. 2001) Santa Cruz pore waters are generally supersaturated with respect to kaolinite (Fig. 13c). The apparent high degree of kaolinite supersaturation in the shallowest soils probably occurs due to significant complexation with DOC. Supersaturation progressively diminishes with increasing depth and approaches near-saturation at depths of about 2 m. This depth range coincides with the argillic horizons containing maximum amounts of kaolinite. Diminished supersaturation reflects progressive decreases in pH and total Al (Fig. 12b and d) which are expected for kaolinite precipitation. Kaolinite, again, progressively supersaturates in the deeper pore waters reaching SI values >5.

The extent of this supersaturation is tempered somewhat by the nature of the Santa Cruz kaolinite, which based on SEM and AFM imaging, is extremely fined grained, with broad 10 Å XRD spectral peaks suggesting relatively poor crystallinity. Thus, the actual solubility of the Santa Cruz kaolinite may be greater and the supersaturation less than for its more crystalline counterpart (Eq. (9) and Yang and Steefel; 2008). In addition, kaolinite is commonly associated with a halloysite precursor with significantly greater solubility (Steefel and Van Cappellen, 1990). The role of kaolinite saturation in the weathering of primary silicates is discussed in greater detail in Maher et al. (2009).

3.4.4. Gibbsite

Of all the potential secondary weathering products considered in the PHREEQC speciation of Santa Cruz pore waters, gibbsite SI values, based on the reaction

$$Al(OH)_{3(gibbsite)} + 3H^+ \rightarrow Al^{3+} + 3H_2O$$
$$\log K_{gibbsite} = 8.87(13.5\,^\circ C) \quad (10)$$

exhibit the least variability with depth and are consistently closest to pore water saturation (Fig. 13d). Near-equilib-

rium, except for pore waters at shallowest depths containing with high DOC, persists in spite of ranges in pore water pH and total Al which vary by more than 2 orders of magnitude (Fig. 12b and d).

Gibbsite is commonly assumed or calculated to be a primary control on Al solubility in many weathering environments (White, 1995; White et al., 2001; Varadachari, 2006). This occurs even when it is not present, as in the case of Santa Cruz, in measurable quantities as a secondary mineral. The reason of this control has never been adequately explained but must be related to fact that gibbsite is relatively soluble, has high nucleation and precipitation rates but is thermodynamically unstable with respect to other secondary phases such as kaolinite and halloysite (Nagy and Lasaga, 1993).

3.5. Cation exchange

In addition to the solid and solute states discussed above, cations also reside on mineral exchange sites and may influence and be influenced by chemical weathering (see additional discussions on cation exchange in Maher et al., 2009). Exchangeable cations, based on acetate extracts of bulk soils, are tabulated in Appendix C. As shown for the SCT 2 and SCT 5 terraces (Fig. 14a and b), exchangeable Ca dominates in the shallowest soils but decreases relative to Mg in the argillic horizons. Calcium gradually increases again relative to Mg in the deeper soils. Both Na and K represent only minor fractions of the total exchangeable cations.

3.5.1. Cation exchange capacities

The dominant exchange substrates are smectite and kaolinite. Smectite is a detrital mineral initially present in the terrace sediments while secondary kaolinite forms from weathering of smectite and primary silicates, principally feldspars (White et al., 2008). These minerals generally exhibit inverse correlations both with depth in individual terraces and in terraces of increasing age (Fig. 14c and d). Additional poorly characterized organic substrates also occur in the shallow soil horizons which also act as cation exchangers. Exchangeable cation abundances generally correlate with surface areas and the abundance of these clays (Fig. 14e and f). BET surface areas closely track kaolinite distributions, whereas, surface areas determined by polyvinylpyrrolidone (PVP) sorption, better measure interlayer exchange associated with smectite (Blum and Eberl, 2004).

With near-neutral pore water pHs (Appendix A), clays can be assumed to be base saturated, making the sum of the measured cations equal to the total cation exchange capacity (CEC). As expected, bulk CECs correlate more closely with smectite than kaolinite (Fig. 14g and h). Specific exchange capacities of smectite and kaolinite were calculated using the SOLVER subroutine in an EXCEL spreadsheet based on measured bulk CEC and mass fraction values of the two clays in each terrace. The default settings in the EXCEL spreadsheet program was used to minimize the sum of squared differences between measured and modeled bulk CEC for a given profile (Fig. 14g and h).

The specific CEC ranges for both smectite (570 to 1060 to meq kg^{-1}) and kaolinite (165 and 354 to meq kg^{-1}) gen-

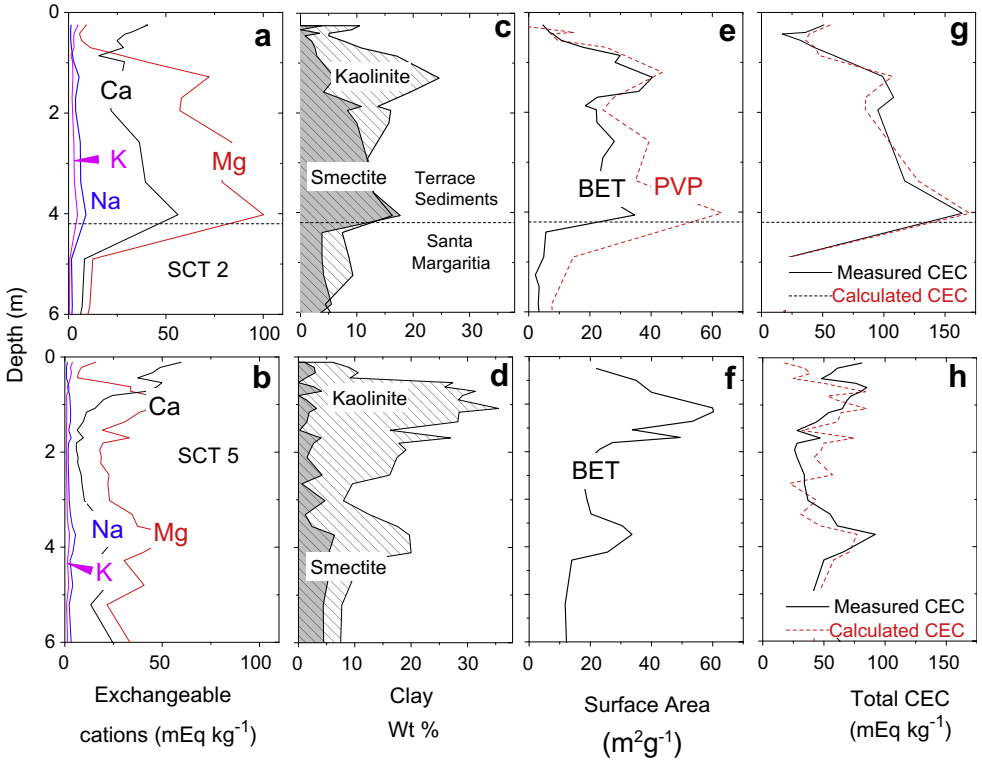

Fig. 14. Sorption characteristics of the SCT 2 and SCT 5 terraces. Vertical distributions of major exchangeable cations (a and b). Distributions of clay minerals (c and d). Bulk soil BET and PVP-measured surface areas (e and f). Measured and calculated cation exchange capacities (g and h).

erally decrease with terrace age (Appendix C). These CECs are comparable with estimates for these minerals calculated using reverse parameter estimation and the CrunchFlow reactive transport model (Maher et al., 2009). While smectite CECs are similar to data reported for pure smectite (Ma and Eggletton, 1999; Coppin et al., 2002), the kaolinite CECs are much higher than those reported for well-crystallized kaolinite (Busenberg and Clemency, 1973; Gaston and Selim, 1991). This discrepancy is probably related to very fine grain sizes and poor crystallinity of the Santa Cruz kaolinite.

3.5.2. Exchange equilibrium

Exchange between sorbed and solution cations is commonly assumed to be comparatively rapid and at equilibrium. Such equilibrium is evident for bivalent cations which dominate CEC totals in the Santa Cruz terraces. For example, when plotted as relative proportions to one another (Ca + Mg = 1), both exchangeable and measured solute Ca/Mg ratios exhibit almost identical variations with depth (Fig. 15a–c).

In the shallowest soils, the proportions of Ca to Mg both on the clay exchangers and in the pore waters are significantly greater than in precipitation and are dominated by the preference of Ca relative to Mg during cycling in the grassland vegetation (Table 3). These proportions progressively decrease with increasing depth in the shallow soils. At the top of the argillic horizon, the proportions of Mg in the pore waters to Mg on the exchange sites are significantly greater than Ca and equal to or greater than that of precipitation (Fig. 15a–c). Below the argillic horizon, these proportions are gradually reversed again, with Ca again becoming more enriched relative to Mg with increasing depth. Similar depth trends are observed between Sr and Mg (data in Appendices A and C).

Corresponding isotopic exchange equilibrium is also evident based on the almost identical co-variation in solute and exchange $^{87}Sr/^{86}Sr$ with depth in the terraces (Fig. 8a–c). Both solute and exchange $^{87}Sr/^{86}Sr$ range from precipitation-dominated radiogenic Sr near the soil surface to less radiogenic plagioclase-dominated Sr at depth. Unlike for Ca/Mg, a lack of fractionation minimizes the role of vegetation on solute and exchange $^{87}Sr/^{86}Sr$ distributions (compare Figs. 15a–c and Fig. 8a–c). The similarities in both pore water/exchange cation ratios and $^{87}Sr/^{86}Sr$ ratios indicate active isotopic exchange throughout the soil col-

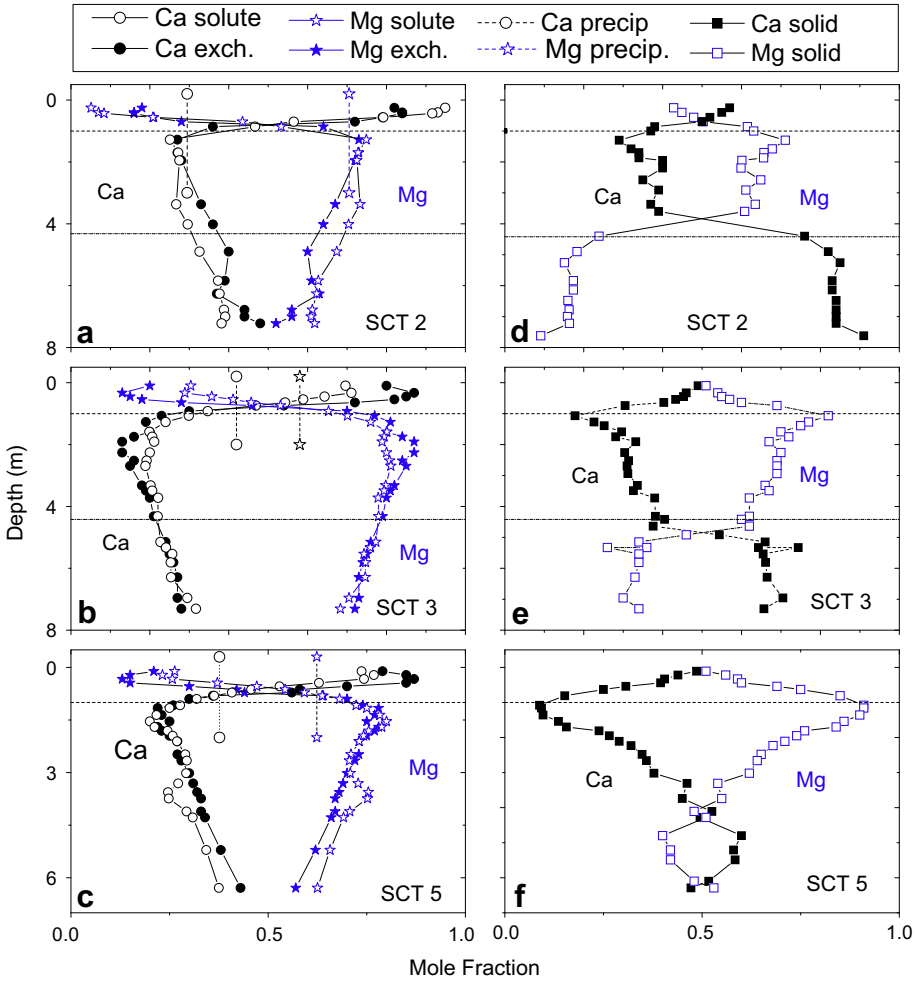

Fig. 15. Relative proportions of Ca and Mg in pore waters and exchange sites (a–c) and in bulk soils (d–f). Points connected by vertical lines are Ca and Mg proportions in precipitation.

umn over the decadal residence times of the pore waters (Table 2).

Selectivity coefficients define the partitioning of cation pairs between the solute and exchange sites. For example, the ratios of Ca/Mg in the pore waters and on the exchanger define the selectivity coefficient, $K_{Ca/Mg}$.

$$K_{Ca/Mg} = \frac{[c_{Ca}/c_{Mg}]_{pore\ water}}{[C_{Ca}/C_{Mg}]_{exchange}} \quad (11)$$

A similar relationship can be defined for other cation pairs such as Ca/Sr.

Significant variability in exchange selectivities in the shallow soils is due to heterogeneities in the exchange substrates, including soil organic matter (Fig. 14c and d). Below the argillic horizon, selectivities are near unity, reflecting equal ratios of Ca, Sr and Mg in the pore waters and on the exchange sites (Fig. 16). Cation selectivities are not particularly sensitive to changes in nature and abundance of both kaolinite and smectite beneath the argillic horizon (Fig. 10c–d). Values of $K_{Ca,Sr/Mg} \approx 1$ are also observed in soils of the Merced chronosequence (White et al. 2005) and are consistent with reported values for smectite (Sposito et al., 1983). Literature values, which indicate a slight preference for Mg over Ca in crystalline kaolinite (Peterson and Coleman, 1965), may not be directly applicable due to the poorly crystalline kaolinite as reflected in the high CEC data reported (Fig 14e and f).

4. DISCUSSION

The hydrochemistry of the Santa Cruz terraces, described in this paper, coupled with previous descriptions of mineral and solid-state element distributions (White et al. 2008), represent one of the most detailed data sets yet obtained for an actively weathering soil regolith. Both the solute and solid-state profiles defined by these data represent geochemical reaction fronts having many characteristics in common with other transport-controlled flow reactions (Ortoleva et al., 1987; Lichtner, 1988; Maher et al., 2006,2009; Lebedeva et al., 2007). Solid-state profiles within the Santa Cruz terraces have been recently described in terms of linear gradient and spreadsheet approximations (White et al., 2008), analytical expressions (Brantley et al., 2008) and numerical simulations using the reactive transport code CrunchFlow (Maher et al., 2009). In the present discussion, the linear estimation approach will be expanded to describe contemporary weathering rates based on the pore water compositions described in this paper. These elemental rates will be compared to long-term weathering based on similar solid-phase element gradients described by White et al. (2008).

Santa Cruz weathering profiles can be approximated by geometric relationships between solute and solid-state weathering rates, gradients and velocities (Fig. 17 and White et al., 2002). The weathering gradients b_{solute} and b_{solid} define respective solute and solid compositional changes with depth. The solutes increase with depth due to cumulative inputs from weathering during the downward advection of water (Fig 17a). Residual solids increase with depth because of decreasing weathering intensities

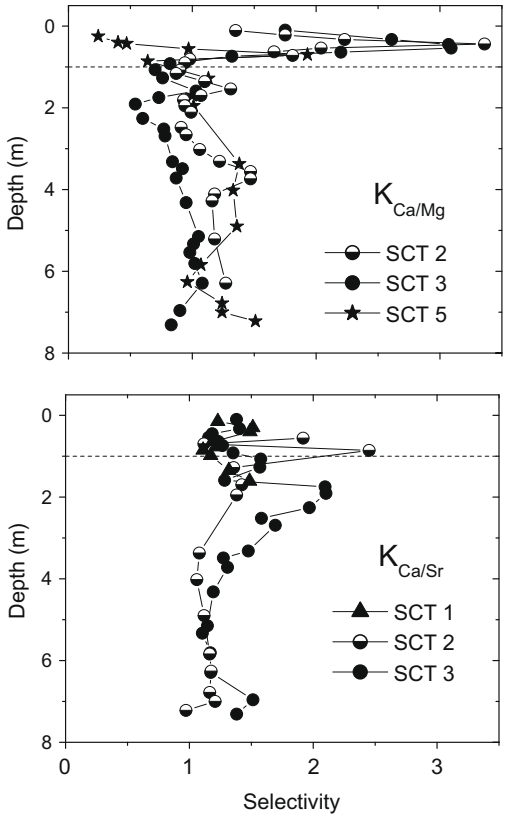

Fig. 16. Exchange selectivities for Ca/Mg and Ca/Sr (Eq. (11)). Dashed horizontal lines are the approximate upper limits of the argillic horizons.

(Fig. 17b). These gradients develop over very different time spans. Solute gradients are produced over the decadal-scale residence times of pore waters at Santa Cruz (Table 2), while the solid-state gradients reflect the cumulative history of weathering (up to 226 kyrs; Perg et al., 2001).

The weathering rates R_{solute} and R_{solid} (mol m^{-2} s^{-1}) in Fig. 17 are mass fluxes normalized to the volumetric surface area of a mineral phase. The solute velocity υ (m s^{-1}) is equivalent to the hydrologic flux q_h *(Eq. (1))*. Under constant hydrologic conditions, the position of the solute weathering front remains spatially fixed within a soil over short fluid residence times (Fig. 17a). The solid-state weathering velocity ω (m s^{-1}) defines the vertical propagation rate of a weathering profile into the protolith as shown schematically in Fig. 17b. With a lack of physical denudation, as approximated in Santa Cruz terraces (Perg et al. 2001), the solid-state weathering velocity (ω) also defines the rate the weathering profiles retreats below the soil surface.

Mineral weathering rates are determined from the weathering velocities and gradients such that (White, 2002).

$$R_{solute} = \frac{q_h}{b_{solute}\beta\ S_v} \quad (12)$$

and

$$R_{solid} = \frac{\omega}{b_{solid}\beta S_v} \quad (13)$$

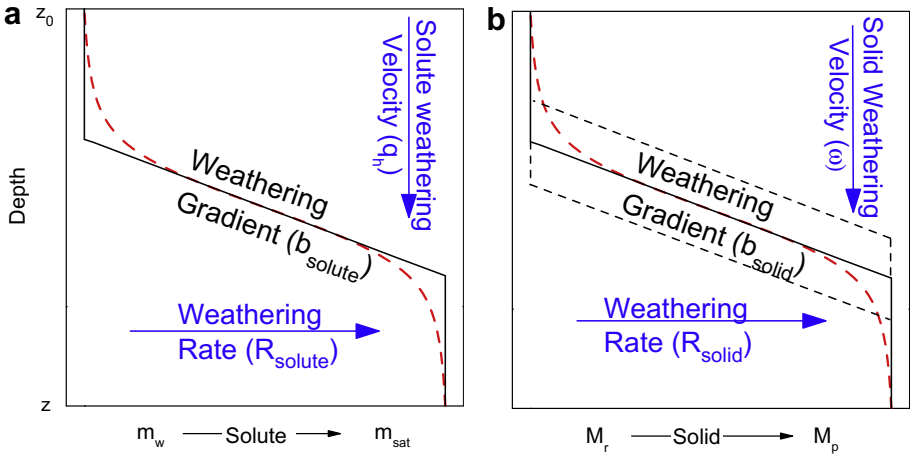

Fig. 17. Schematic showing the relationships between solute and solid-state weathering rates, gradients and velocities (Eqs. (12) and (13)); after White, 2002). The soil surface is defined as z_0, m_w is the net solute composition derived from weathering and m_{sat} is the solute composition in thermodynamic equilibrium with the protolith. M_r and M_p are the respective solid regolith and protolith compositions. Dashed lines denote progressive advance of the solid-state profile with time. Sigmoid-shape curves are representations of the non-linear aspects of weathering profiles (White et al., 2008; Brantley et al., 2008).

where β is the stoichiometric coefficient relating the elemental concentrations to mineral abundances and S_v is the volumetric surface area of the mineral phase ($m^2\ m^{-3}$). Note that the solute flux density q_h (Eq. (1)), unlike the advective velocity v (Eq. (2)), is independent of porosity which is implicitly contained in volumetric surface area term S_v.

All of the terms in Eqs. (12) and (13) are considered as being constant in the following analysis, which results in linear approximations of the weathering profiles. The solute and solid-state weathering profiles shown in Fig. 17 are approximated by three linear segments. The vertical gradient at shallow depth corresponds to the zone in which the residual reactive phase has been completely depleted ($M_r = 0$), while the deep vertical gradient corresponds to the protolith composition (M_p) where weathering has not yet commenced. The weathering rates in these zones are zero, corresponding to infinitely steep gradients (Eqs. (12) and (13)).

In the zone of active mineral weathering, the linear approximations to the profiles are described by the gradients b_{solute} and b_{solid}, which reflect the relative magnitudes of the weathering rates and velocities (arrows in Fig. 17). The units for b_{solute} and b_{solid} are defined as $m^4\ mol^{-1}$ when employing the convention of plotting the depth on the vertical axes (Fig. 17). As previously noted by Ortoleva et al. (1987) and Lichtner (1988), increasing rates of reaction produce thinner profiles and shallower gradients while decreasing rates will produce thicker profiles and steeper gradients.

The linear approximations, described by Eqs. (12) and (13) are compared in Fig. 17, to idealized sigmoid-shaped curves whose geometries are commonly considered representative of many natural weathering profiles. The asymptotic aspect of such curves at shallow depth is generally ascribed to changing relationships between mineral surface-to-volume ratios at low residual mineral concentrations (White et al., 2008; Brantley et al., 2008). At greater depths, the asymptotic approaches to the protolith concentrations are attributed to the increasing importance of the reaction affinity, as further discussed in the companion paper of Maher et al. (2009).

The geometry of weathering profiles can also be defined in terms steady versus non-steady state over time. As discussed by Lichtner (1988), White et al. (2008) and Brantley et al. (2008), a reaction front remains at pseudo-steady state when it is bounded by conditions such that a shallow depth a residual mineral is completely depleted ($M_r = 0$ at $z = 0$) and at some greater depth where the regolith approaches the original protolith concentration ($M_r = M_p$). Under these conditions, the shape of the profiles is geometrically fixed with all points along the gradient which move downward at a constant weathering velocity (Fig. 17).

Non-steady geometries may also apply to weathering profiles. If during the initial stages of weathering, the residual concentration at the surface z_0 continues to decrease with time ($M_r \neq 0$), the shape of the weathering profile will continue to evolve and the mass loss in the upper parts of the profile will continue to decrease until the condition $M_r = 0$ at $z = 0$ is met. At greater depths, both the reaction rate and the rate at which the profile geometry approaches the boundary condition $M_r = M_p$ progressively decrease and tend toward zero as a result of reaction affinities associated with both primary and secondary minerals. As demonstrated by Maher et al. (2009) such inhibitions promote weathering profiles that continually evolve over longer times and to greater depths than based on the linear approximation discussed here.

Interestingly, the simple linear approximations, represented by Eqs. (12) and (13), have proven to be surprisingly robust in comparisons to field weathering rates generated by more inclusive non-linear analytical and numerical approaches (see comparisons of Santa Cruz rates calculated in White et al., 2008; Brantley et al., 2008; Maher et al., 2009). One apparent reason for this agreement is that many of the more detailed aspects

considered in these approaches tend to cancel each other out when the overall weathering rate is considered (White et al., 2008). This is shown in the comparison of the linear versus non-linear profiles in Fig. 17 in which opposing asymmetries in shallow and deep parts of the profile are negated after integrating under curves to produce total weathering losses.

The advantages of the linear approximation approach lies in its simple geometric interpretation of field-measured weathering profiles which can then be used to estimate both contemporary and long-term chemical weathering rates. The disadvantage of such approximations, as evident in the more comprehensive approach described by Maher et al. (2009), lies in its inability to evaluate the effects of additional parameters such as the role of secondary mineral supersaturation and the approach to equilibrium suggested by experimental data (Burch et al., 1993; Gautier et al., 1994; Hellmann and Tisserand, 2006). However, it must be pointed out that such more detailed interpretations are often based on as yet unresolved issues related to kinetic theory, in addition to poorly constrained field data.

4.1. Contemporary plagioclase weathering rates based on solute Na and Si gradients

Weathering profiles, plotted in terms of volumetric solute concentrations m_w of Na and Si (mol m^{-3}) are shown in Fig. 18. Solutes in deeper portions of the Santa Margarita Sandstone in SCT 2 and SCT 3 are not included in the linear regression fits due to the diminished rate of plagioclase weathering (Figs. 6 and 11). These deep zones approximate the vertical protolith gradients shown in Fig. 17 and indicate thermodynamic saturation with respect to plagioclase (albite) as suggested in Fig. 13a. Solute gradients are not considered for the youngest SCT 1 terrace due to the shallow nature of the weathering profile and to seasonal ground water intrusion.

The slopes of regression fits to the Na and Si data correspond to the weathering gradients contained in Eq. (12) and range between $b_{Na,solute} = 4.5$ and $20.6\ m^4\ mol^{-1}$ and between $b_{S,isolute} = 6.6$ and $11.4\ m^4\ mol^{-1}$ (Table 4). Shallower gradients signify more rapid increases of solute Na and Si with depth and, therefore, more rapid plagioclase

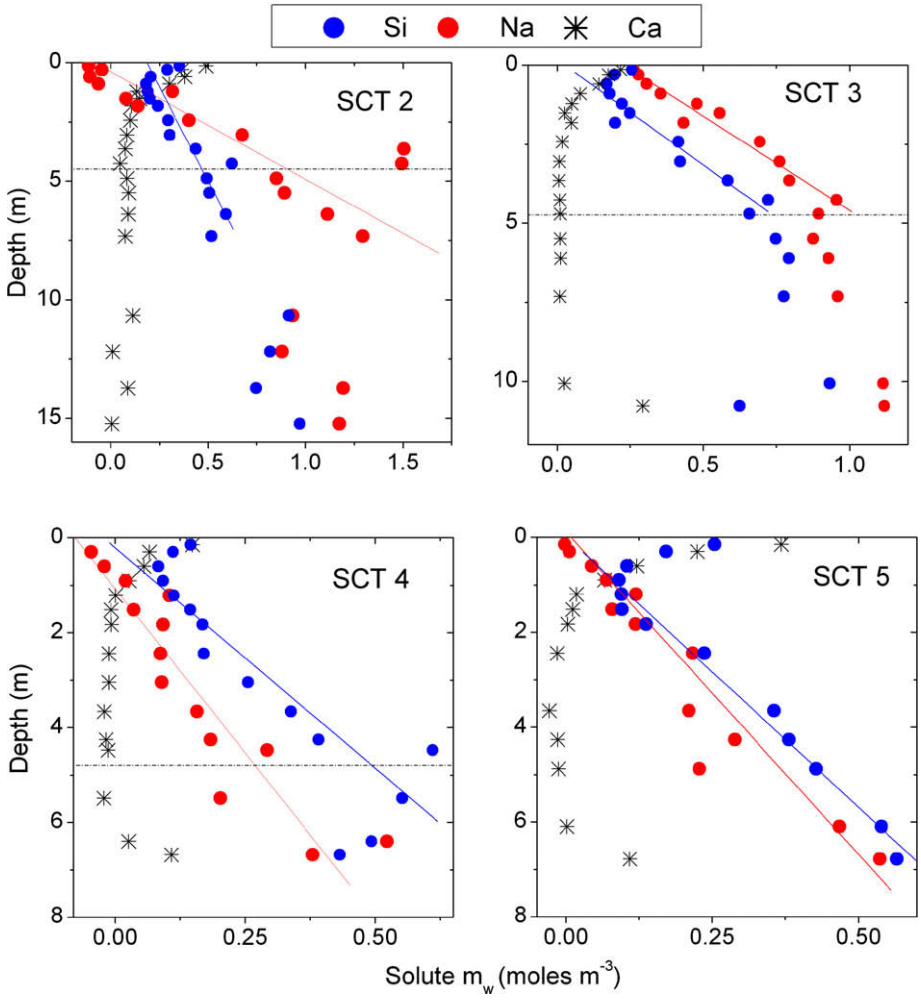

Fig. 18. Solute weathering profiles. Data points are net average pore waters distributions corrected for precipitation (Eq. (4)). Diagonal lines are linear regressions defining the weathering gradients $b_{Na,solute}$ and $b_{Si,solute}$ contained in Eq. (12) and Table 4. Horizontal lines are the contacts between the terrace sediments and the Santa Margarita Sandstone (not present in SCT 5).

Table 4
Parameters used to calculate plagioclase weathering rates.

	SCT 1	SCT 2	SCT 3	SCT 4	SCT 5	
Age	65	90	137	194	226	kyrs
Gradient $b_{Na,solute}$	nd	4.53	5.95	20.55	13.59	m/(mol/m^{-3})
Gradient $b_{Si,solute}$	nd	7.39	6.65	9.30	11.40	m/(mol/m^{-3})
Gradient $b_{Na,solid}$	0.0008	0.0032	0.0037	0.0046	0.0058	m/(mol/m^{-3})
Granient $b_{Ca,solid}$	0.0013	0.0084	0.0097	0.0088	0.0150	m/(mol/m^{-3})
Flux q_s	0.062	0.173	0.170	0.218	0.088	m yr^{-1}
Surface area S_v	7.46E+05	3.85E+05	4.41E+05	5.38E+05	4.55E+05	m^2 m^{-3}
Soluble plag m_{solute}	nd	0.92	1.25	1.62	1.26	mol m^{-3}
Total plag M_{total}	2.13E+03	2.33E+03	1.87E+03	2.36E+03	1.91E+03	mol m^{-3}
Velocity ω (geometric)	1.89E−05	3.97E−05	3.26E−05	3.24E−05	2.46E−05	m yr^{-1}
Velocity ω Eq. ((19))	nd	6.86E−05	1.14E−04	1.50E−04	5.82E−05	m yr^{-1}
β_{Na}	0.73[a]	0.73	0.72	0.71	0.70	
β_{Ca}	0.27[a]	0.27	0.28	0.29	0.30	
β_{Si}	1.46[a]	1.46	1.44	1.42	1.40	
Rate $R_{Na,solute}$	nd	4.31E−15	2.85E−15	8.82E−16	6.46E−16	mol m^{-2} s^{-1}
Rate $R_{Si,solute}$	nd	1.32E−15	1.27E−15	9.75E−16	3.85E−16	mol m^{-2} s^{-1}
Rate $R_{Na,solid}$[b]	1.37E−15	1.38E−15	8.750E−16	5.86E−16	4.20E−16	mol m^{-2} s^{-1}
Rate $R_{Ca,\ solid}$[b]	2.23E−15	1.44E−15	8.62E−16	7.45E−16	3.82E−16	mol m^{-2} s^{-1}
Rate $R_{plag,\ model}$	8.00E−16	1.40E−15	8.00E−16	1.00E−15	4.80E−16	mol m^{-2} s^{-1}

[a] Assumed from SCT 2
[b] Solid rates based on geometric weathering velocities

weathering. Precipitation fluxes and Cl balances were used to estimate hydraulic fluxes (Eq. (1)) which ranged between $q_h = 0.062$ and 0.218 m yr^{-1} (Table 4). The stoichiometric coefficient β values in Eq. (12) for Na and Si were determined by microprobe analyses of individual plagioclase grains from the different terraces (White et al., 2008). The Si coefficients were also modified to reflect the fact that Si released as a result of plagioclase weathering is also incorporated into secondary kaolinite (compare Eqs. (7) and (9)). Resulting coefficients ranged between $\beta_{Na} = 0.70$–0.73 and the $\beta_{Si} = 1.40$–1.46 (Table 4).

The surface area S_v in Eq. (12) is equal to product of the mass of residual mineral present in a volume of regolith M_r (kg m^{-3}) and the specific surface area defined per unit of mineral mass S_{min} (m^2 kg^{-1}).

$$S_v = M_r \cdot S_{\min} \tag{14}$$

The residual mass decreases with decreasing depth in a profile while specific mineral surface area may be expected to increase, reflecting decreases in residual grain sizes and increases in surface pitting and roughness (White et al., 1996). These opposing trends may result in relatively small variations in volumetric surface areas across significant portions of a weathering profile and may be responsible for the commonly observed pseudo-linear nature of many weathering gradients (Lichtner, 1988). In the following calculations, M_r is set equal to one half of that of the initial protolith M_p (Fig. 17), which corresponds to the depth in the profile undergoing maximum rates of weathering (see Maher et al., 2009). The specific mineral surface area S_{min} is calculated from the geometric surface area based on average particle diameters and normalized to a BET equivalent value using age-dependent surface roughness factors estimated by White and Brantley (2003). Values for S_v are listed in Table 4.

The plagioclase weathering rates, based on the solute Na gradients $b_{Na,solute}$ (Fig. 18 and Eq. (12)) generally increase with decreasing terrace age from $R_{Na,solute} = 0.64$–4.31×10^{-15} mol m^{-2} s^{-1} (Table 4). These values are slightly higher than plagioclase weathering rates based on solute Na distributions previously reported for a comparable soil chronosequence developed on river terraces near Merced, California ($R_{Na,solute} = 0.31$–0.72×10^{-15} mol m^{-2} s^{-1}; White et al., 2005). Higher rates are ascribed to higher precipitation and fluid fluxes at Santa Cruz compared to Merced. Corresponding rates based on solute Si gradients in the Santa Cruz terraces ($R_{Si,solute} = 0.38$–1.32×10^{-15} mol m^{-2} s^{-1}) are only slightly lower than those determined for Na and also exhibit a consistent decline with soil age. Unlike Na, solute Si is only an approximate surrogate for plagioclase weathering because it is potentially generated by other silicates and is assumed to be stoichiometrically incorporated into only kaolinte as a secondary phase.

4.2. Determination of contemporary plagioclase weathering rates based on solute $^{87}Sr/^{86}Sr$ gradients

In a manner analogous to elemental distributions, the solute $^{87}Sr/^{86}Sr$ trends in Fig. 8 constitute weathering profiles which reflect the ratio of the fluid flux to the dissolution rate of plagioclase. If these distributions represent steady-state conditions, the depth dependence of the pore fluid (denoted $^{87}Sr/^{86}Sr_{\ pw}\ (z)$) can be determined using the approach of Maher et al. (2003):

$$\frac{d^{87}Sr/^{87}Sr_{solute}(z)}{dz} = \frac{\theta m_{solute} R_{sr} S_m c_{Sr,solute}}{q_h C_{Sr,solid}} \times \left[{}^{87}Sr/^{86}Sr_{plag}(z) - {}^{87}Sr/^{86}Sr_{solute}(z)\right] \tag{15}$$

where $c_{Sr,solute}$ and $C_{Sr,solid}$ are the corresponding solute and solid-state elemental Sr concentrations at depth z, q_h is water flux (Eq. (1)) and θ is the volumetric water content (Eq. (3)). The mass of fluid to solid mass M is calculated from the relationship

$$m_{solute} = \frac{\rho_{bulk}(1-\phi)}{\rho_{water}\theta} \tag{16}$$

where ρ_b is the bulk density ρ_{solute} is the fluid density and φ is the porosity (Appendix A).

This approach assumes that the bulk of the Sr is derived from plagioclase dissolution, an assumption that is supported by the close correlation between the plagioclase abundances and solute $^{87}Sr/^{86}Sr$ (Fig. 8). Measured values for $c_{Sr,solute}$ and $C_{Sr,solid}$ and values used to calculate m_{solute} are contained in Appendices A and B and in White et al. (2008) , Eq. (15) was fit to the data by using the calculated hydraulic fluxes and then varying the bulk weathering rate (R_{sr}) to minimize the misfit between model and measured values for $^{87}Sr/^{86}Sr$. Assumed model values are provided in Fig. 19.

$^{87}Sr/^{86}Sr$ in the SCT 1 solute profile has a shallower gradient, requiring faster weathering rates relative to those of the older terraces, which have roughly similar flow rates and weathering rates. Within individual terraces, a decrease in the value of R_{Sr}/q_h at depth was required to match the subtle change in slope of the pore water $^{87}Sr/^{86}Sr$. The Sr model also suggests that mineral dissolution is required over the length of the measured profiles in order to sustain the observed $^{87}Sr/^{86}Sr$ of the pore waters, consistent with the undersaturation of plagioclase in the pore waters (Maher et al., 2009). The Sr isotopic data provide another

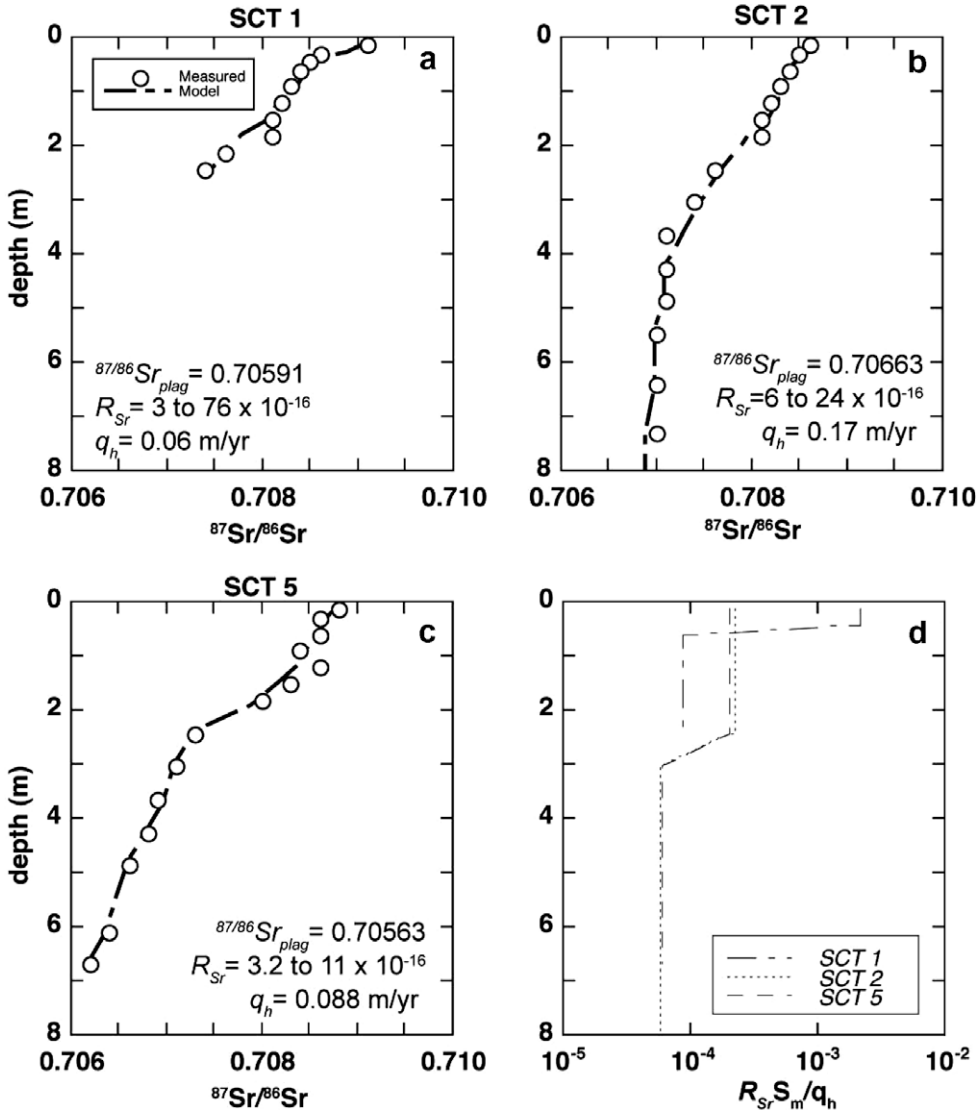

Fig. 19. Model fit to pore water $^{87}Sr/^{86}Sr$ data for SCT 1, 2 and 5 terraces using Eq. (15) (a–c). Assumed model values for the dissolving $^{87}Sr/^{86}Sr$ (r_s), the weathering rate constant (R_{Sr}, mol/m^2/s), and the flow rate (q_h) are provided for the corresponding terrace profile. The maximum and minimum weathering rates for the profile are also provided. (d) Profiles correspond to R_{Sr}/q_h for each terrace. Plagioclase specific surface area was assumed to be $S_m = 1.94$ m^2/g for all terraces.

means of calculating contemporary weathering rates from solute data and yields rates that are similar to rates calculated using major element solute fluxes and solid profile evolution (see Table 4).

4.3. Long-term elemental weathering rates based on solid-state gradients

In a previous paper in this series, White et al. (2008) used plagioclase distributions, based on XRF analyses, to calculate corresponding weathering rates. In this section, the parallel case is presented for calculating weathering rates based on solid-state element distributions. While these two rates should be linked by the stoichiometric coefficients for plagioclase (β_j values in Table 4), the calculations are derived from independent measurements of mineral and element distributions, in addition to assumptions involving the relative reactivity of different mineral phases. An interesting aspect of solid-state element distributions, now discussed, is that they can be directly compared to solute distributions of these same elements described in the preceding sections.

4.3.1. Determining solid-state weathering gradients

Solid-state gradients are defined by the residual elemental distribution with depth in a weathering profile (Fig 17). Such element distributions do not equate directly to the measured concentrations because of selective removal or addition of other elements by weathering and physical dilation and/or compaction which change the thickness of a profile. Solid-state elemental distributions in the Santa Cruz terraces, along with requisite correction factors based the approaches previous described in Brimhall et al. (1991), Chadwick et al. (1990) and Egli and Fitze (2000), are contained White et al. (2008).

The resulting solid-state Na and Ca weathering profiles are plotted for the terraces SCT 2–5 in Fig. 20. A comparable profile for SCT 1 was generated but is not shown. Sodium and Ca at the shallowest depths in SCT 2, 3 and 4 terraces are negative, indicating that the employed corrections do not accurately describe the complex interactions involving biologic perturbations and eolian deposition in these soil horizons.

As shown by the regression fits, residual Na and Ca exhibit relatively consistent linear increases over significant

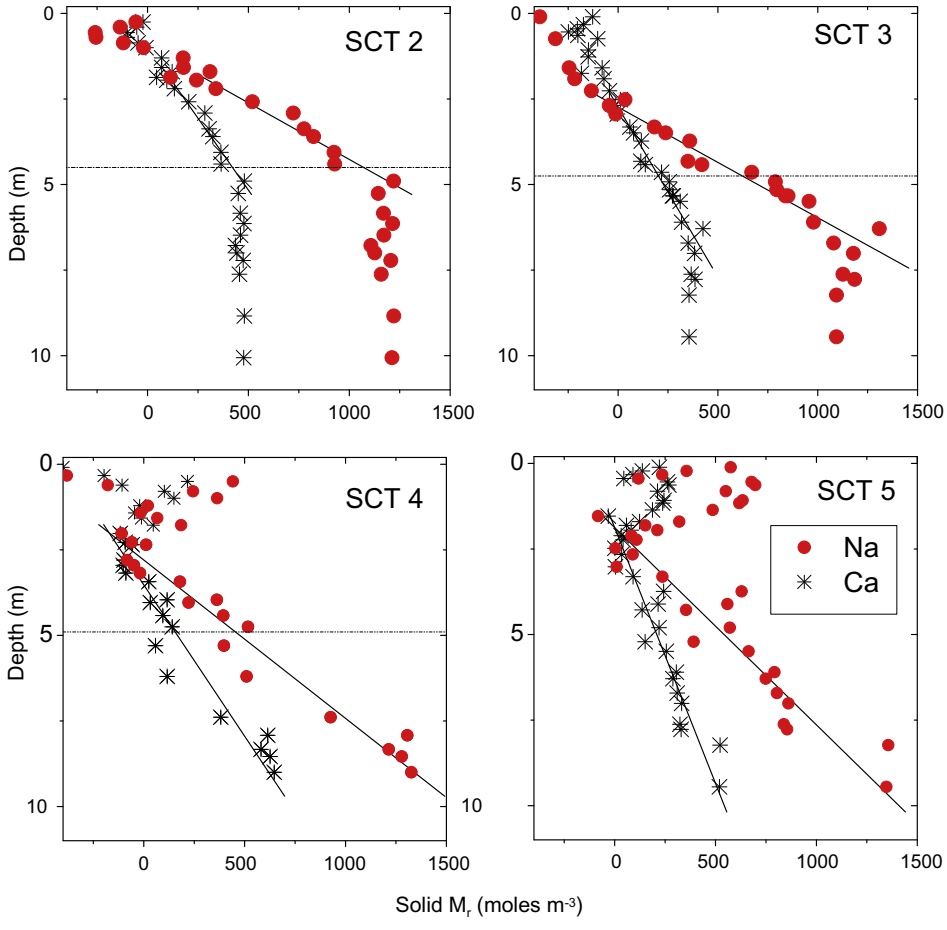

Fig. 20. Solid-state Na and Ca weathering profiles. Residual elemental masses M_r are calculated from measured solid-state compositions and corrections contained in White et al. (2008). The solid lines, based on linear regressions fits, define the weathering gradients $b_{solid,Na}$ and $b_{solid,Ca}$ (Eq. (12) and Table 4). Horizontal lines are the contacts between the terrace sediments and the Santa Margarita Sandstone (not present in SCT 5).

depth intervals (Fig. 20) which correspond to the solid-state weathering gradients schematically shown in Fig. 17. The similarity in solid-state weathering Na and Ca profiles (Fig. 20) is contrasted with the dissimilarity between the solute Na and Ca profiles (Fig. 18). A direct comparison of solid-state and solute Si profiles is not possible because, although abundant quartz does not contribute significantly to the pore water Si, it comprises a significant portion of solid-state Si.

Eolian inputs are clearly evident in the older SCT 4 and SCT 5 profiles based on the increases in residual Na and Ca above the argillic horizons (Fig. 20). Such inputs most likely occurred during the last low level sea-level stand (12–15 ka) which exposed much of the coastal margin west of Santa Cruz and is responsible for paleo sand dunes present along Monterey Bay to the south of Santa Cruz (White et al., 2008). The role of eolian input on development of the weathering profiles is further addressed in a companion paper (Maher et al., 2009). Extrapolation of the weathering gradients from deeper in the profiles implies that, prior to these relative recent eolian additions, plagioclase was essentially totally depleted in the shallow soils, i.e., $M_r = 0$ at $z_0 = 0$ (Fig. 20). Finally, the near-vertical Na and Ca gradients at depth in the SCT 2 and SCT 3 terraces document a lack of further plagioclase weathering at depth in the Santa Margarita Sandstone. This is in agreement with similar conclusions based on solute Na and $^{87}Sr/^{86}Sr$ Si profiles (Figs. 6 and 8) as well as the presence of thermodynamically saturated state of the pore waters based on albite solubilites (Fig. 13).

The linear gradients for Ca ($b_{Ca,solid} = 0.13–1.5 \times 10^{-2}$ m^4 mol^{-1}) are larger and steeper than for Na ($b_{Na,solid} = 0.81–5.8 \times 10^{-3}$ m^4 mol^{-1}) because lesser amounts of Ca are lost from plagioclase ($\beta_{Ca} < \beta_{Na}$ in Table 4). As expected, the solid-state Na gradients are several orders of magnitude smaller than the corresponding solute Na gradient, signifying much larger changes in solid-state Na relative to solute Na concentrations with terrace depth (Table 4).

4.3.2. Determining solid-state weathering velocities and rates

Several approaches can be used to estimate solid-state velocities (ω in Eq. (13)) under specific weathering conditions. In the absence of physical erosion, the average weathering velocity can be determined by dividing depth of the soil profile by the age of the soil surface. For the Santa Cruz profiles this is done by finding the inflection point of the best-fit sigmodial curves generated the spreadsheet spread calculator for plagioclase distributions in each terrace (see Fig. 16, White et al., 2008). The depth of this inflection point, which corresponds to the maximum rate of reaction (also see Maher et al., 2009), is then divided by the respective cosmogenic age of the terrace surface (Perg et al., 2001). The resulting solid weathering velocities ranged from 1.89 to 3.97 $\times 10^{-5}$ m yr^{-1} for the five terraces (Table 4). As would be expected, the solid-state velocities are many orders of magnitude slower than the solute velocities which correspond to the hydrologic flux (3.7–6.4 $\times 10^{-1}$ m yr^{-1} in Table 4). This scale difference emphasizes the fact that thousands of pore water volumes have infiltrated through the weathering profiles during their development.

An alternate weathering scenario is that of geomorphic steady state (note this is different than geometric steady state discussed previously), in which case the rate of physical denudation of the regolith surface is equal to the rate at which the weathering profile penetrates into the protolith (Pavich, 1986; Riebe et al., 2003). The weathering velocity can then be equated to this denudation rate which is determined independently from techniques such as cosmogenic ^{10}Be distributions. This approach to defining weathering velocities was used in determining biotite weathering rates in a granitic saprolite at Panola, Georgia (White et al., 2002).

A more general approach to estimating solid-state weathering velocities was suggested by White et al., 2008. Under steady state, transport-limited conditions, the weathering velocity is equal at each point along the profile and is directly proportional to the fluid flux

$$\omega = q_h \cdot \left[\frac{m_{sol}}{M_p}\right] \tag{17}$$

where m_{sol} (mole m^{-3}) is the mass of mineral that can be dissolved into a volume of saturated pore waters divided by M_p, the total amount of mineral present in the protolith. In first Santa Cruz paper, White et al. (2008) calculated solid-state velocities based on the reaction of albite to kaolinite (combining Eqs. (8) and (9). In a concurrent paper Maher et al. (2009), consider the plagioclase/kaolinite reaction under non-equilibrium conditions where plagioclase dissolution is kinetically coupled to kaolinite precipitation via decreasing reaction rates as reaction affinities of both minerals trend toward saturation.

An alternate possibility is that the reaction of albite to kaolinite involves a metastable intermediate or precursor phase controlling one or more solute species. The chief candidate is gibbsite which appears to constrain Al solubilites in most of the Santa Cruz pore waters (Fig. 13d) such that

$$NaAlSi_3O_{8(albite)} + H^+ + H_2O \rightarrow Na^+ + 3SiO_2 \ + Al(OH)_{3(gibbsite)}$$
$$logK_{eq} = -5.82\,(13.5\,^\circ C) \tag{18}$$

The amount of plagioclase solubilized in a volume of pore water, based on measured pH and assumed closed system release of Na and Si varies between 0.92 and 1.62 mol/m^3 of solution (Eq. (18) and Table 4). Combining these masses (m_{sol}) with the initial masses of plagioclase present in the terrace protolith (M_{total}) (Table 4) and the fluid flux (Table 1) results in weathering velocities of $\omega = 0.58–1.50 \times 10^{-4}$ m yr^{-1}. These velocities are only about a factor of 3 greater than velocities determined from the profile geometries $\omega = 0.18–0.397 \times 10^{-4}$ m yr^{-1}, suggesting that gibbsite metastability may partially control plagioclase solubility and weathering.

4.4. Comparisons of contemporary and long-term weathering

Comparing contemporary and past silicate weathering rates is important in addressing a number of important issues such as soil sustainability, climate change and global CO_2 drawdown. Most studies addressing this issue have

compared long-term elemental or mineral changes, such as in soil profiles, with estimates of contemporary weathering based on solute exports from associated watersheds, an approach which is subjected to scaling issues (see review by White, 2008). The present paper, along with a previous study of the Merced chronosequence (White et al., 2005) represents the first efforts to directly compare the long-term and contemporary silicate weathering rates using solute and solid-state element distributions within single soil profiles.

The extent to which weathering rates vary with time is dependent on both intrinsic characteristics of the mineral phase, e. g., defect densities and surface area, and extrinsic characteristics of the weathering environment, e. g., fluid compositions, solution reaction affinities and biologic activity (White and Brantley, 2003). Considerable debate exists as to whether contemporary weathering rates, influenced by changes in these characteristics, are comparable to average long-term geologic rates. Some studies conclude that present-day weathering, impacted by processes such acidic deposition and/or warmer, wetter climates, are significantly faster than long-term past weathering rates (April et al., 1986; Kirkwood and Nesbitt, 1991; Cleaves, 1993). However other studies have concluded that within the errors involved, contemporary and average long-term weathering rates are essentially indistinguishable (Stonestrom et al., 1998; White et al., 1998; White et al., 2002; White et al., 2005).

4.4.1. Comparison of weathering gradients

Based on the geometric interpretations summarized in Fig. 17, the solute and solid-state weathering profiles should be directly related under steady state weathering conditions. Assuming constant weathering rates and surface areas, Eq. (12) can be equated to Eq. (13) such that

$$\left[\frac{q_h}{\omega}\right] \cdot \left[\frac{b_{solid}}{b_{solute}}\right] = 1 \tag{19}$$

where the product of the ratio of the weathering velocities and inverse ratio of the weathering gradients is equal to one. The extent to which this condition is met, i.e., the product of the measured parameters on the left side of Eq. (19), approach unity is a gauge of the correctness of this steady-state weathering assumption.

The values for Eq. (19), based on the velocities and gradients contained in Table 4, are plotted in Fig. 21. The two data sets correspond to the different approaches used to calculate the solid-state weathering velocity, i.e. the geometric and transport-limited estimates (Fig. 17 and Eq. (17)). When considering the large differences in the scales of the parameters involved (see Table 4), the fact that the values generated by Eq. (19) are bounded by factors that are <3 of each other for each terrace generally supports steady state weathering for plagioclase. An interesting observation is that while values calculated by assuming transport-limited velocities are consistently lower than those based on geometric velocities, the trends in the two data sets converge closer to unity in the older terraces (Fig. 21). This situation may reflect the fact that weathering is deeper and profiles are better developed, providing better estimates of the respective solute and solid-state gradients.

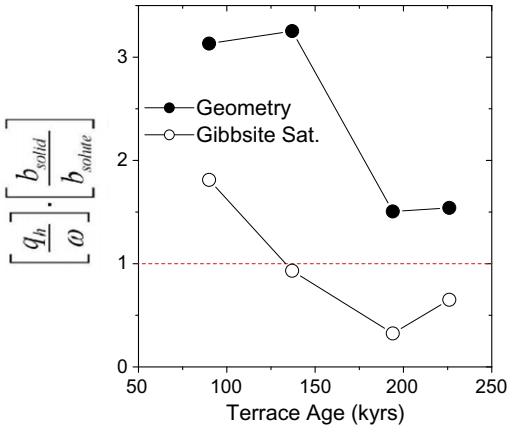

Fig. 21. Comparison of present day and long term plagioclase weathering based on the respective ratios of weathering gradients and velocities for terraces of different ages (Eq. (19)). Separate data sets reflect solid-state weathering velocities based on measured profile depths (geometric) and assumed transport-limited weathering based Eq. (17).

4.4.2. Comparison of contemporary and long-term weathering rates

Plagioclase weathering rates based on solute Na and Si (Eq. (12)), solid/solute $^{87}Sr/^{86}Sr$ (Eq. (15) and Fig. 19) and solid-state Na and Ca (Eq. (13) and Fig. 20) are plotted together as functions of terrace age in Fig. 22. Also included are plagioclase weathering rates previously determined using the spreadsheet calculator of White et al. (2008). Taken together, this data set represents the most comprehensive characterization of field-based mineral weathering rates yet compiled for a single weathering environment. In a companion paper, Maher et al. (2009) pre-

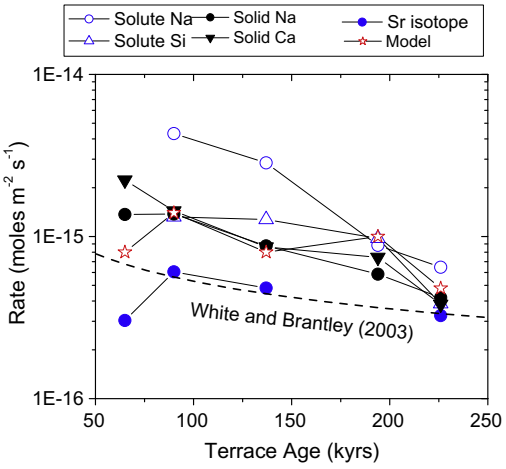

Fig. 22. A comparison of contemporary and long-term plagioclase weathering rates based on solute and solid-state elemental and $^{87}Sr/^{86}Sr$ gradients. Also included are previously estimated plagioclase rates based on a spreadsheet calculation (White et al., 2008) and a power function fit to a tabulation of natural weathering rates (White and Brantley, 2003).

sents additional results which reconcile these field rates to laboratory-derived rates.

Plagioclase weathering rates for any single terrace fall within an order of magnitude of each other with differences becoming significantly less for the older SCT 4 and SCT 5 terraces (Fig. 22). This convergence may reflect more accurate measurement of weathering parameters in the older terraces which contain deeper and better defined profiles. The principal outliers are weathering rates based on solute Na profiles in the younger terraces which may reflect an underestimation of the marine aerosol input to sites closest to the ocean. Systematically lower rates based on the Sr isotope mass balance (Eqs. (15) and (16)) may reflect the failure to account for the inputs of a more radiogenic component in K-feldspar.

Plagioclase weathering rates, based on any single approach, generally exhibit modest declines with increasing terrace age, an effect has been previously documented for other chronosequences (Taylor and Blum, 1995; White et al., 1996; Hodson and Langan, 1999) and for compilations of single weathering environments of different ages (White and Brantley, 2003). Due to the relatively short time scale of weathering at Santa Cruz, (65–226 kyrs), declines in weathering with age is less pronounced than in some other chronosequences such as at Merced, which has a time span of 10–3000 kyrs (White et al., 1996; White et al., 2005). The Santa Cruz rate data generally parallels a power law curve describing the general decline with time of average plagioclase weathering rates derived from a large number of sources (White and Brantley, 2003). The overall Santa Cruz rates are generally faster than these averages, probably reflecting higher average temperatures and precipitation than for many of weathering environments.

The similarities in weathering gradients and rates shown in Figs. 21 and 22 produce a consistent pattern of plagioclase weathering. This consistency implies that environmental conditions over a decadal time scale reflected in present day solute weathering rates for plagioclase are representative of long term average rates which are responsible for the solid-state soil profiles developed over hundreds of thousands of years. Environmental changes over intermediate time frames such as in climate or vegetation cover undoubtedly occurred but their impacts on the distribution of the selected weathering components were either minor compared to the resolution of the plagioclase rate calculations or else these such changes were simply averaged out over the long term weathering history of the terraces such that they are approximated by contemporary conditions.

4.5. Inconsistencies in base cation weathering

Significant inconsistencies exist in the solute distributions of bivalent Ca, Sr and Mg, which exhibit essentially no inputs from chemical weathering within the soil profiles (Fig. 7). These results run counter to the assumption that, as in the past, present day weathering of plagioclase and smectite is actively mobilizing these base cations into solution. This discrepancy requires invoking one or more processes that are selectively removing these cations at rates equal to or greater than the rates of chemical weathering. Primary silicates, in additional to detrital smectite, are weathering to kaolinite, a relatively barren phase for base cation incorporation. Biological uptake of these mineral nutrients by the present day grassland vegetation is limited to shallow rooting depths, precluding removal to depths to which solute Ca, Sr and Mg are depleted. The only remaining possibility is exchange onto clay mineral surfaces.

An important but often unrecognized characteristic of soils are the very large differences in the sizes of bulk soil, exchange and pore water reservoirs. The masses of a species in the bulk soils is generally between one and two orders of magnitude larger than on the exchange sites, which, in turn, are one to two orders of magnitude larger than in the pore waters (Fig. 23). Such mass differences are also related to the relative rates at which these reservoirs evolve with time as a result of weathering. The solid-state changes very slowly with time (10^6 yrs) while the solute compositions change very rapidly with time (10^1 yrs). The exchange reservoir is expected to evolve over intermediate time frames. For example masses of Ca and Sr on the exchange sites represent about 10^3 yrs of plagioclase weathering, neglecting external inputs.

The exchange reservoir acts as a filter through which any direct comparison of solute and solid-state weathering rates must be made. This filter is relatively insensitive to weakly sorbed weathering components such Na or Si or for Sr isotopes which are not fractionated by exchange processes. Such insensitivity explains the consistency in solute and solid-state weathering rates based on these components (Fig. 22). However, for more strongly sorbed base cations, the role of exchange processes is much more important. Under steady state conditions, reflecting constant weathering and consistent external inputs, principally from precipitation, the three reservoirs are expected to be at "equilibrium" in the chronosequence soils (Fig. 23). The exchange reservoir reflects gradual weathering-induced inputs from the bulk soils which in term are reflected in changes in the pore water compositions.

Equilibrium is evident between exchange and pore water base cations as shown by the strong co-variation Ca, Sr,

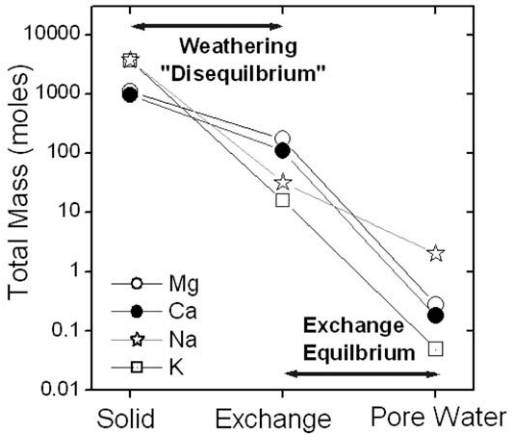

Fig. 23. Total masses of elements contained in the SCT 5 profile. Data from Appendices A and C and from White et al, 2008.

Mg and $^{87}Sr/^{86}Sr$ isotopic ratios (Figs. 8 and 15). In contrast, concentrations of exchangeable and pore base cations do not reflect long-term trends in solid-state compositions produced by chemical weathering. This is most readily demonstrated in Fig. 15 by comparing the relative consistency in the Ca/Mg exchange and pore water ratios in each terrace profile (Fig. 15a–c) with the solid-state Ca/Mg ratios which exhibit consistent declines with terrace age reflecting the fact that residual Mg- phases are ultimately retained longer in the terraces than the Ca-phases (Fig. 15d–f). In addition, the absolute abundances of solid-state Ca and Mg decrease with terrace age, weathering trends which should increase the relative importance of precipitation inputs to the exchange and pore Ca/Mg ratios in the older terraces. However, the Ca/Mg exchange and pore water profiles are essentially identical in all the terraces and do not correspond to precipitation (Fig. 15a–c). The state of base cation "disequilibrium" between the solid-state weathering and exchange reservoirs is contrasted to the state of equilibrium between the exchange and pore water reservoirs (Fig. 23).

If base cation exchange and pore compositions do not correlate with long-term weathering trends or with contemporary precipitation inputs, the question arises as to what process do they reflect? A lack of correlations between solute and exchange Ca/Mg and $^{87}Sr/^{86}Sr$ and long-term declines of plagioclase weathering was previously documented for the Merced chronosequence. For the extreme case at Merced, exchange Ca/Mg and $^{87}Sr/^{86}Sr$ ratios, inductive of plagioclase weathering inputs, persisted in a 3 million years old terrace in which residual plagioclase was completely absent. White et al. (2005) suggested that continued elevated solute and exchange Ca/Mg ratios resulted from past external inputs of Ca possibly as a result of dust. Bullen et al. (1997) attributed corresponding Sr isotope disequilibrium in the Merced soils to a decreasing exchange efficiency factor that correlated with increased physical isolation of previously equilibrated exchange sites, probably by formation of protective layers such Fe-oxhydroxides.

An additional possibility, to be addressed in more detail in a subsequent Santa Cruz paper, is that the exchange reservoir is currently in the process of slowing re-equilibrating from different past environmental conditions, analogous to that projected for long-term soil base cation recover from acid precipitation (Driscoll et al., 2005). In the case of Santa Cruz, exchange disequilibrium may be driven by changes in the intensity and depth of mineral nutrient cycling caused by a past transition from a forest to a present day grassland ecosystem, as implied by Holocene pollen records near Santa Cruz (Adam et al., 1981). In any case, the selection of pore water species in weathering rate calculations, even in "natural" systems, requires a detailed understand of the past and present weathering environment.

5. CONCLUSIONS

The marine terrace chronosequence, near Santa Cruz California, provides an ideal natural laboratory in which to study silicate weathering rates and to assess the importance of various intrinsic and extrinsic controls. This paper builds on descriptions of the bulk soil compositions, elemental distributions and long-term feldspar weathering rates presented in a previous paper in this series (White et al., 2008) by detailing hydrologic flow paths and solute distributions and by developing parallel approaches for characterizing both contemporary and long-term rates based on weathering gradients.

The Mediterranean climate at Santa Cruz produces a strong seasonal variation in precipitation, which drives growth cycles in the grassland community and controls the evapotranspiration's role on pore water solutes. Solute fluxes from precipitation are relatively constant across the terraces, reflecting the compensating effects of increasing rainfall with elevation coupled with decreasing amounts of sea-spray derived solutes with increasing distance from the coast. Argillic soil horizons, produced by precipitation of secondary kaolinite, provide major controls on hydrologic fluxes. These horizons, which increase in thickness with increasing soil age, impede percolation, producing perched ground water during the rainy season and dampening seasonal variations in soil moisture and tension in the underlying deep unsaturated zones. Chloride mass balances permit the calculation of fluid fluxes which indicate decadal-scale pore water residence times in the terraces. These rates mean that many thousands of pore water volumes have passed through the terraces since their deposition.

Significant biological activity, reflected in soil organic matter, is generally confined to soil horizons above the argillic horizon. Biological cycling impacts the shallow distributions of major mineral nutrients, including Ca and K, which are present in higher concentrations than Na and Mg, which dominate in precipitation. In spite of large inputs from coastal precipitation, Cl-corrected solute Na and K, in addition to Si, increase with depth, indicating that feldspar weathering contributes significantly to pore water compositions. This is also documented by mixing trends between radiogenic seawater-like $^{87}Sr/^{86}Sr$ in shallow soils with non-radiogenic Sr contributed from plagioclase at depth. However, solute concentrations of Sr, in addition to Ca, decrease in the deeper soils, indicating that plagioclase weathering inputs are overridden by other processes that selectively remove these cations without $^{87}Sr/^{86}Sr$ fractionation.

The ratios of pore water and exchange Ca, Mg and Sr are essentially identical, resulting in selectivity coefficients close to unity for substrates dominated by varying proportions of detrital smectite and secondary kaolinite. On a short-term basis, buffering by the much larger cation-exchange reservoir explains the lack of apparent Ca and Sr increases in pore waters relative to Na and Si, which are not strongly sorbed. However, over long times, Ca and Sr inputs decrease with diminishing amounts of residual plagioclase. When coupled with continued precipitation inputs, solute and exchange Ca/Mg and Sr/Mg ratios are expected to decline and $^{87}Sr/^{86}Sr$ to become more radiogenic. However, such shifts are not apparent in that both the cation and isotopic ratios remain relatively constant in terraces

of increasing age. Discrepancies between cation and $^{87}Sr/^{86}Sr$ ratios and long-term mineral weathering trends have been explained elsewhere as possible combinations of declining exchange efficiencies in older soils coupled with long-term external inputs, possibly in the form of dust. Documented changes in the vegetation succession could also periodically reset the exchange reservoirs of the Santa Cruz terraces.

Solute Na and Si distributions approximate linear weathering gradients, and when coupled to the hydraulic fluxes estimated from Cl mass balances, can be used to calculate plagioclase weathering rates. Additional plagioclase rates are based on solute $^{87}Sr/^{86}Sr$ distributions. These approximations are extended to solid-state gradients involving Na and Ca by assuming that the solid-state weathering velocity is saturation-limited. Therefore, the plagioclase weathering velocity is directly proportional to the hydraulic flux density, and inversely proportional to the amount of plagioclase initially present. Thermodynamic saturation of deep pore waters with respect to plagioclase is confirmed by using pH calculated from measured alkalinity and soil gas CO_2.

Parallel approaches, using both solute and solid-state elemental distributions in the Santa Cruz terraces provides one of first direct comparisons between short term weathering, reflecting fluid residence times of one to two decades and average long-term weathering rates, spanning the entire age range of terrace development. Multiple plagioclase weathering rates for any single terrace are within an order of magnitude of each other with no consistent differences in rates calculated from solute or solid gradients. Rates are generally faster than average compilations for field-based plagioclase weathering, suggesting environmental conditions, such as higher precipitation, may influence weathering. Conversely, decreases in rates with terrace age implying that conditions intrinsic to plagioclase, such as declining surface reactivity, is also influencing reaction rates.

ACKNOWLEDGMENTS

We thank the Rangers and staff at Wilder State Park, specifically Tim Hyland for his help in the field and Stephanie Mills of Laguna Ranch who provided access for the study. Mark Huebner of the U.S. Geologic Survey provided the anion analyses. We would like to acknowledge the following colleagues for helpful discussions and for assistance in the field: Jennifer Harden, Jennie Munster, Carrie Maseillo, Mark Waldrop, Daniel Bain and Susanne Anderson in addition to acknowledging insights and suggestions provided by Jacque Schott and two anomalous reviewers of the manuscript. Funding was provided by the National Research Program of the Water Resources Discipline of the U.S. Geological Survey.

APPENDIX A

Representative compositions of precipitation (precip), surface water (sw), pore water (pw) and groundwater (gw) of the Santa Cruz Terrraces. Data as μM except as noted. Depths as meters.

Depth	Type	Date	pH	Alk	Na	Mg	Si	K	Ca	Rb	Sr	Cl	NO^3	SO_4
SCT1 Age = 65 kyrs; Site locationLat = N36.95411°; Long = N122.02651° Elev. = 6 m														
00.00	precip.	12/29/2003	5.79	0	270	29	1.1	5.9	7.1	0.0000	0.06	321	5.7	19
0.15	pw	12/2/2003	6.00	125	3283	1009	509	290	1830	0.0554	5.75	4288	4469	333
0.30	pw	1/16/2003	5.92	112	1960	357	461	33.0	308	0.0103	1.19	1636	1299	122
0.45	pw	12/18/2002	6.33	260	1195	355	563	35.0	501	0.0092	1.65	1410	914	204
0.60	pw	1/16/2003	5.77	229	3405	156	582	24.0	94.2	0.0076	0.44	2640	440	283
0.91	pw	1/16/2003	6.20	139	3276	243	888	13.5	95.4	0.0055	0.64	2008	1428	200
1.22	pw	1/16/2003	5.70	86	2043	147	543	17.4	59.7	0.0053	0.37	1365	657	142
1.52	pw	1/16/2003	5.76	105	1640	109	549	14.3	65.7	0.0044	0.34	1004	511	154
1.79	pw	1/16/2003	7.02	1486	3690	154	840	19.3	92.0	0.0064	0.43	1749	657	200
2.13	pw	1/16/2003	6.32	329	2024	87	784	8.4	33.5	0.0032	0.24	1185	551	100
2.44	pw	1/16/2003	6.92	1553	2805	651	631	11.1	308	0.0054	1.99	2065	685	267
2.67	gw	7/1/2003	6.73	2855	6724	565	—	41.9	374	0.0068	1.53	4344	260	604
SCT 2 Age = 90 kyrs Site location Lat = N 36.967968°; Long = W 122.085047°; Elev. = 67 m														
0.00	precip.	4/17/2003	5.46	0	155	20	1.1	4.3	12.4	0.000	0.05	206	1.1	17
0.00	sw	4/2/2003	6.81	397	999	227	418	32.3	1160	0.003	1.6	3418	216	191
0.15	pw	1/6/2003	5.40	15	597	317	383	230	795	0.0934	2.24	1173	1257	292
0.30	pw	1/29/2002	6.12	77	387	67	277	100	212	0.0400	0.59	463	328	65
0.60	pw	2/26/2002	6.56	148	409	79	239	127	201	0.0590	0.62	485	231	100
0.91	pw	2/26/2002	6.69	239	608	381	151	32.9	364	0.0123	1.81	812	885	108
1.22	pw	2/26/2002	6.83	407	715	513	169	10.4	179	0.0042	1.23	632	714	188
1.52	pw	2/26/2002	6.82	287	694	575	181	26.1	264	0.0111	1.70	914	914	142
1.83	pw	2/26/2002	6.60	198	618	374	170	45.2	163	0.0179	1.07	530	685	167
2.44	pw	2/26/2002	6.68	200	905	543	271	9.5	155	0.0036	1.35	722	714	300
3.05	pw	2/26/2002	6.61	181	1419	350	332	13.8	116	0.0040	0.95	733	685	358
3.65	pw	2/26/2002	6.75	289	2116	280	445	19.4	97.3	0.0050	0.88	688	685	625
4.27	pw	2/26/2002	6.49	73	2141	179	635	26.4	63.6	0.0074	0.59	711	685	596

Appendix A. (*continued*)

Depth	Type	Date	pH	Alk	Na	Mg	Si	K	Ca	Rb	Sr	Cl	NO^3	SO_4
4.88	pw	2/26/2002	6.79	181	1905	284	509	21.3	124.6	0.0049	1.05	1365	1171	42
5.49	pw	2/26/2002	6.76	164	1434	169	519	20.0	77.3	0.0032	0.66	530	400	413
6.40	pw	1/6/2003	6.23	212	1770	160	626	28.7	95.1	0.0106	0.74	643	568	416
7.22	pw	2/26/2002	6.84	206	2292	214	592	29.0	125.6	0.0042	1.04	891	1142	392
12.19	pw	5/30/2003	6.64	328	1377	68	829	27.0	32.5	0.0050	0.18	631	528	79
13.72	pw	11/18/2003	6.23	331	2260	159	812	50.2	142	0.0054	0.88	1128	1299	48
15.24	pw	5/30/2003	6.80	359	1750	105	972	57.3	34.3	0.0170	0.23	739	571	225
SCT3 Age = 137 kyrs Site location Lat = N 36.976366°; Long = W 122.077621°; Elev. = 110 m														
0.00	precip.	2/27/2003	5.89	0	181	22.6	2.4	5.5	15.5	2E-04	0.03	231	12	23
0.00	sw	3/12/2002	7.30	513	1066	227	402	22.5	347	0.0171	1.46	1292	300	167
0.15	pw	2/12/2002	6.16	49	281	83	214	102.6	185	0.0630	0.56	153	551	61
0.30	pw	3/12/2002	5.84	54	337	65	175	66.0	190	0.0392	0.59	141	571	56
0.60	pw	2/12/2002	6.09	165	280	103	151	32.0	139	0.0173	0.61	339	177	41
0.60	pw	3/12/2002	6.03	92	274	76	137	24.4	102	0.0166	0.48	282	178	39
0.91	pw	2/12/2002	5.63	52	346	183	149	10.6	98.7	0.0121	0.65	496	300	37
0.91	pw	3/12/2002	5.64	58	367	139	147	8.2	77.1	0.0083	0.53	392	271	41
1.22	pw	3/12/2002	5.47	10	439	117	170	7.3	37.3	0.0054	0.31	384	236	52
1.52	pw	2/12/2002	5.38	32	568	140	208	5.8	36.1	0.0043	0.34	519	286	44
1.52	pw	3/12/2002	5.35	7	545	128	214	3.6	32.1	0.0033	0.33	505	307	46
3.05	pw	2/12/2002	5.86	73	755	37	380	5.1	8.4	0.0033	0.09	496	207	28
4.27	pw	3/12/2002	5.96	60	967	34	755	6.9	7.1	0.0035	0.09	606	250	95
5.49	pw	2/12/2002	6.31	116	883	30	733	15.4	11.1	0.0045	0.09	564	200	63
6.10	pw	10/25/2001	5.95	109	919	33	699	16.3	8.7	0.0040	0.07	733	86	68
7.32	pw	5/30/2002	6.56	158	1011	32	849	13.2	13.2	0.0039	0.10	787	74	66
10.1	pw	6/5/2003	6.28	323	1144	63	894	24.0	26.1	0.0052	0.20	911	40	60
10.9	gw	12/11/2002	6.50	401	1159	274	631	43.3	316	0.0471	1.58	1537	357	48
SCT4 Age = 193 kyrs Site location Lat = N 36.983609°; Long = W 122.077006°; Elev. = 159m														
0.00	precip.	3/21/2003	5.80	0	125	15	0	3.0	9.0	0.001	0.04	152	14	14
0.00	sw	3/12/2002	7.27	381	423	94	252	40.1	127	0.0509	0.61	420	3.6	40
0.15	pw	12/29/2003	5.66	40	460	152	131	102.5	336	0.1356	1.22	1317	95	30
0.30	pw	4/22/2003	5.88	50	254	83	106	20.5	26.1	0.0147	0.24	291	34	61
0.60	pw	5/30/2002	6.93	158	162	55	141	56.2	42.0	0.0504	0.25	110	25	68
0.91	pw	5/30/2002	5.99	60	219	64	111	24.1	24.5	0.0179	0.21	203	30	63
1.22	pw	5/30/2002	5.80	46	308	45	135	8.1	17.4	0.0085	0.16	234	18	72
1.52	pw	5/30/2002	5.55	41	284	39	144	5.3	19.5	0.0068	0.13	279	11	40
1.83	pw	5/30/2002	5.56	36	323	44	149	10.1	12.4	0.0073	0.14	279	7.7	61
3.05	pw	5/30/2002	5.91	55	320	38	250	6.9	7.5	0.0040	0.13	296	30	21
3.66	pw	5/30/2002	5.63	63	471	19	321	5.4	3.8	0.0035	0.08	381	29	32
4.26	pw	5/30/2002	6.98	143	499	39	387	14.0	12.1	0.0123	0.17	412	14	32
4.48	pw	5/30/2002	6.06	259	629	34	575	16.8	15.1	0.0107	0.18	406	6.2	55
5.49	pw	5/30/2002	5.94	200	815	47	523	30.3	31.2	0.0178	0.28	787	3.0	29
6.40	pw	5/30/2002	5.94	357	1247	72	519	43.7	91.9	0.0244	0.56	874	250	85
6.87	gw	4/8/2004	5.94	723	1009	152	408	54.5	189	0.0262	0.80	748	74	71
SCT5 Age = 226 kyrs Site location Lat = N 36.99466°; Long = W 122.133071°; Elev. = 189 m														
0.00	precip.	3/12/2003	5.64	0	145	18	0	4.3	12.7	0.002	0.04	186	1.7	16
0.00	sw	3/12/2002	7.27	381	423	94	252	40.1	127	0.0509	0.61	420	3.6	40
0.15	pw	1/10/2002	6.41	228	457	176	271	156.6	524	0.0748	1.10	866	14.0	135
0.30	pw	1/10/2002	6.60	543	314	92	180	91.4	344	0.0472	0.66	604	15.1	52
0.60	pw	3/26/2002	6.53	247	448	147	83	10.5	116.1	0.0079	0.46	471	6.6	125
0.90	pw	3/26/2002	6.19	115	417	195	78	13.2	96.8	0.0062	0.51	361	92.8	202
1.20	pw	3/26/2002	5.83	44	493	131	88	2.8	42.3	0.0038	0.27	522	20.7	141
1.52	pw	3/26/2002	5.14	13	555	183	86	3.8	51.4	0.0036	0.39	635	21.4	175
1.83	pw	3/26/2002	5.63	88	494	111	118	2.7	35.9	0.0026	0.29	454	3.9	124
2.44	pw	3/26/2002	5.63	55	720	73	194	12.7	24.8	0.0097	0.26	652	119	58
3.05	pw	3/26/2002	5.47	10	1292	152	263	22.5	63.3	0.0146	0.60	1100	643	20
3.65	pw	3/26/2002	5.95	57	1129	98	324	21.3	38.2	0.0123	0.42	1306	60	25
4.27	pw	3/26/2002	6.20	90	1126	109	357	23.0	46.8	0.0156	0.50	1205	141	29
4.88	pw	3/26/2002	6.33	112	1189	120	404	29.3	57.5	0.0139	0.57	1331	106	32
5.49	pw	12/18/2002	5.85	183	854	48	540	30.8	30.7	0.0230	0.27	806	3.7	30
6.40	pw	12/18/2002	6.23	337	1313	75	533	44.6	82.2	0.0252	0.57	928	228	85
6.70	gw	4/17/2003	7.26	358	1664	222	598	34.2	141	0.0034	1.31	1489	557	24

APPENDIX B

Pore water and exchange $^{87}Sr/^{86}Sr$.

Depth m	Pore Water $^{87}Sr/^{86}Sr$	Pore Water Sr[a]	Depth m	Acetate exchange $^{87}Sr/^{86}Sr$
SCT 1				
0.15	0.70797	2.147	0.15	0.70807
0.3	0.70797	2.260	0.30	0.70803
0.45	0.70789	1.729	0.40	0.70797
0.61	0.70759	0.811	0.65	0.70765
0.91	0.70733	0.707	0.85	0.70756
1.22	0.70750	0.733	1.35	0.70739
1.52	0.70743	0.360	1.61	0.70728
1.83	0.70722	0.281	2.08	0.70735
2.13	0.70712	0.346	2.50	0.70758
2.44	0.70691	nd	2.70	0.70757
precip	0.70910	0.065		
plag	0.70591			
SCT 2				
0.15	0.70860	1.504	0.13	0.70842
0.30	0.70851	1.116	0.33	0.70841
0.61	0.70840	1.310	0.41	0.7084
0.91	0.70834	1.334	0.85	0.7083
1.22	0.70821	1.053	0.99	0.70827
1.52	0.70808	1.220	1.29	0.70817
1.83	0.70807	0.900	1.70	0.70787
2.44	0.70759	1.078	1.95	0.70773
3.05	0.70736	0.916	2.54	0.70743
3.66	0.70710	0.822	3.37	0.7072
4.27	0.70710	0.641	4.90	0.70709
4.88	0.70707	1.088	6.26	0.70738
5.49	0.70702	0.726	7.22	0.70695
6.40	0.70698	0.751		
7.32	0.70696	1.001		
precip	0.70907	0.055		
plag	0.70660			
SCT 3				
0.15	0.70869	0.700	0.1	0.70862
0.30	0.70863	0.530	0.33	0.70863
0.60	0.70874	0.650	0.54	0.70859
0.91	0.70863	0.520	0.92	0.70845
1.52	0.70832	0.290	1.59	0.70826
1.83	0.70824	0.460	1.75	0.70818
2.43	0.70774	0.180	2.69	0.70746
3.05	0.70744	0.080	2.94	0.70739
3.65	0.70797	0.080	3.32	0.70728
4.27	0.70690	0.090	3.49	0.70715
5.49	0.70715	0.090	4.92	0.70669
6.10	0.70704	0.100	5.54	0.70675
7.32	0.70695	0.090	6.29	0.70674
precip	0.70916	0.051		
plag	0.70620			
SCT 5				
0.15	0.70878	0.830	0.22	0.70854
0.30	0.70864	0.500	0.33	0.70862
0.61	0.70862	0.540	0.63	0.70846
0.91	0.70844	0.510	0.9	0.70841
1.22	0.70856	0.310	1.16	0.70836
1.83	0.70796	0.260	1.81	0.70785
2.44	0.70729	0.350	2.48	0.70732
3.05	0.70713	0.610	3.02	0.70701
3.65	0.70690	0.410	3.31	0.70687
4.27	0.70680	0.490	3.74	0.7067
4.88	0.70658	0.580	4.28	0.70661
6.10	0.70640	0.329	6.29	0.70613
precip	0.70942	0.008		
plag	0.70563			

Appendix B. (*continued*)

[a] Sr in μMol

APPENDIX C

Cation exchange data for Santa Cruz terraces. Depths in meters. Smectite (Sm) and kaolinite (kao) as wt %. CEC as mmol kg^{-1}. Specific mineral exchanges calculated by EXCEL.

Depth	Sm	Kao	Na	Mg	K	Ca	Sr	CEC
SCT 1								
0.15	2.78	0.10	1.4	8.0	2.2	20.3	0.081	60.3
0.30	2.06	3.68	1.1	5.4	1.2	14.0	0.062	41.3
0.40	2.98	4.75	1.4	3.8	0.9	14.1	0.066	38.2
0.65	9.78	7.86	12.2	32.6	2.1	16.1	0.115	111.9
0.77	11.09	7.12	16.1	43.5	2.5	19.9	0.156	145.7
0.85	13.85	3.20	16.5	43.2	2.3	19.7	0.151	144.8
0.98	12.18	2.24	20.8	50.1	1.6	20.5	0.167	163.9
1.10	10.97	2.01	21.1	42.0	1.6	17.6	0.147	142.2
1.35	7.80	7.83	24.2	38.6	1.4	16.4	0.125	135.8
1.61	8.68	2.59	15.7	24.9	1.0	10.4	0.081	87.5
2.50	7.53	1.86	4.2	15.6	1.0	14.6	0.092	65.9
2.70	9.10	1.48	5.8	17.8	1.3	18.8	0.113	80.5
Smectite 1060 mmol kg^{-1}; Kaolinite = 353 mmol kg^{-1}								
SCT 2								
0.25	3.84	10.55	1.3	4.5	4.9	20.3	0.073	56.0
0.40	3.37	5.06	1.0	3.0	3.0	15.9	0.059	42.0
0.43	0.83	4.96	1.1	2.8	2.8	14.5	0.053	38.6
0.56	2.04	7.67	1.2	3.4	2.6	12.4	0.049	35.5
0.70	2.64	10.85	1.4	5.6	2.8	14.1	0.068	43.8
0.86	2.91	17.14	2.1	13.9	1.2	7.8	0.095	46.8
1.28	6.13	24.61	5.4	36.1	2.2	13.6	0.128	107.3
1.70	10.75	13.68	3.6	29.0	1.8	10.8	0.104	85.2
1.95	8.26	16.01	3.6	28.6	2.0	10.9	0.105	84.8
3.37	12.30	12.76	6.2	39.4	3.0	19.7	0.183	127.9
4.02	17.66	16.34	8.9	50.1	4.6	28.1	0.251	170.4
4.90	3.77	8.58	1.5	6.2	0.7	4.1	0.037	22.9
5.84	5.48	4.40	1.9	5.4	0.5	3.5	0.030	20.4
6.26	2.16	6.11	1.4	4.2	0.4	2.5	0.022	15.2
6.78	3.83	2.25	1.1	4.0	0.4	3.2	0.029	15.9
7.00	2.33	4.43	1.3	4.1	0.5	3.3	0.031	16.7
7.22	3.46	7.79	1.1	3.7	0.4	3.4	0.027	15.8
Smectite 725 mmol kg^{-1}; Kaolinite = 220 mmol kg^{-1}								
SCT 3								
0.10	4.74	4.25	1.2	5.2	4.2	20.8	0.090	57.6
0.33	13.89	0.09	0.6	2.3	2.6	15.0	0.066	38.0
0.45	12.20	0.22	0.6	2.4	2.3	13.0	0.059	33.8
0.54	9.01	0.01	0.6	2.5	1.6	10.9	0.054	29.0
0.64	11.53	1.46	0.6	3.8	1.5	9.9	0.057	29.5

Appendix C. (*continued*)

Depth	Sm	Kao	Na	Mg	K	Ca	Sr	CEC
0.92	18.43	1.65	1.8	15.0	1.6	6.6	0.059	46.8
1.07	26.19	2.59	2.6	17.8	1.9	5.3	0.060	50.8
1.27	23.36	0.00	2.4	13.2	1.1	3.2	0.042	36.3
1.59	17.66	2.14	2.1	11.8	1.0	3.0	0.041	32.8
1.75	20.06	3.07	2.5	13.0	1.1	2.5	0.043	34.7
1.91	12.26	4.16	1.9	11.2	0.8	1.6	0.032	28.4
2.26	18.67	5.71	2.8	16.7	1.1	2.5	0.051	42.4
2.52	10.35	6.93	3.3	18.5	1.2	3.4	0.060	48.3
2.69	15.80	3.25	3.7	19.8	1.2	3.6	0.067	51.9
3.32	15.76	4.99	4.9	21.8	1.1	4.7	0.073	59.2
3.49	17.65	7.06	5.9	22.7	1.3	5.4	0.077	63.6
3.72	17.10	6.33	5.7	21.8	1.2	5.4	0.075	61.5
4.32	12.12	7.21	6.4	26.9	1.5	7.2	0.091	76.5
5.15	10.35	4.22	2.9	16.5	0.8	5.1	0.056	47.0
5.33	3.89	4.14	3.0	16.7	0.9	5.4	0.059	48.1
5.54	8.81	3.31	3.0	16.8	0.9	5.7	0.059	48.9
5.81	11.28	2.48	2.8	16.2	0.7	5.6	0.060	47.2
6.29	8.23	2.36	3.1	18.4	1.0	6.7	0.066	54.6
6.96	6.53	2.87	3.3	19.3	1.3	7.3	0.072	58.1
7.31	5.83	4.41	3.4	19.3	1.4	7.5	0.071	58.5
Smectite 573 mmol kg^{-1}; Kaolinite = 165 mmol kg^{-1}								
SCT 5								
0.11	1.09	6.13	1.3	7.9	3.9	29.8	0.079	80.8
0.22	2.80	9.01	0.9	4.2	2.9	24.5	0.060	61.4
0.33	3.01	10.64	0.8	3.5	3.4	22.5	0.054	56.3
0.44	1.28	9.20	0.8	3.3	2.8	18.7	0.049	47.7
0.63	2.81	26.05	2.1	17.0	1.2	23.7	0.103	84.7
0.72	4.12	31.36	2.0	16.9	1.7	21.1	0.095	79.8
0.90	1.36	28.36	2.7	22.6	0.9	9.9	0.078	68.8
1.08	3.19	35.46	2.9	22.6	0.9	7.7	0.068	64.7
1.16	1.88	28.52	3.0	19.2	0.9	5.6	0.054	53.6
1.36	1.47	28.33	2.9	15.5	0.9	4.7	0.046	44.5
1.54	0.24	16.32	2.0	9.7	0.8	3.2	0.030	28.5
1.70	4.04	27.04	3.2	16.6	1.0	4.8	0.053	47.0
1.81	2.67	17.81	1.9	9.8	0.7	2.9	0.034	28.2
1.95	2.09	19.08	1.7	9.0	0.8	2.9	0.033	26.4
2.11	1.51	17.54	1.7	9.4	0.9	3.4	0.037	28.3
2.48	4.21	16.20	1.9	11.4	0.9	4.2	0.050	34.1
2.66	0.63	9.56	2.0	11.0	1.0	4.4	0.052	34.0
3.02	4.68	7.97	2.2	11.5	1.1	5.0	0.059	36.5
3.31	1.21	12.60	2.9	17.3	1.2	7.9	0.097	54.6
3.56	2.36	17.60	3.9	18.7	1.7	9.0	0.108	61.2
3.74	6.44	19.74	5.5	28.2	2.4	13.6	0.164	92.0
4.11	5.38	19.95	4.1	20.1	1.9	9.9	0.121	66.2
4.28	5.90	11.04	2.6	15.2	1.3	7.9	0.096	50.4
5.21	4.45	7.67	2.2	10.8	0.9	6.7	0.078	38.2
6.29	4.52	7.43	3.6	18.9	1.7	14.3	0.158	72.0
Smectite 637 mmol kg^{-1}; Kaolinite = 184 mmol kg^{-1}								

REFERENCES

Adam D. P., Byrne R. and Luther E. (1981) A late Pleistocene and Holocene pollen record from Laguna de Las Tancas, Northern Coastal Santa Cruz County, California. *Madrono* **28**, 255–272.

Amacher M. C., Henderson R. E., Breithaupt C. L., Seale C. L. and LaBauve J. M. (1990) Unbuffered and buffered salt methods for exchangeable cations and effective cation exchange capacity. *Soil Sci. Soc. Am. J.* **54**, 1036–1042.

Anderson R. S., Densmore A. L. and Ellis M. A. (1999) The generation and degradation of marine terraces. *Basin Res.* **11**, 7–19.

April R., Newton R. and Coles L. T. (1986) Chemical weathering in two Adirondack watersheds: past and present-day rates. *Geol. Soc. Am. Bull.* **97**, 1232–1238.

Arnórsson S. and Stefánsson A. (1999) Assessment of feldspar solubility constants in water in the range 0° to 350 °C at vapor saturation pressures. *Am. J. Sci.* **299**, 173–209.

Bastviken D., Thomsen F., Svensson T., Karlsson S., Sanden P., Shaw G., Matucha M. and Oberg G. (2007) Chloride retention in forest soil by microbial uptake and by natural chlorination of organic matter. *Geochim. Cosmochim. Acta* **71**, 3182–3192.

Boudot J. P., Maitat O., Merlet D. and Rouiller J. (1996) Occurrence of non-monomeric species of aluminum in undersaturated soil and surface waters: consequences for the determination of mineral saturation indices. *J. Hydrol.* **177**, 47–63.

Blum A. E. and Eberl D. D. (2004) Measurement of clay surface areas by polyvinypyrrolidone (PVP) sorption and its use for quantifying illite and smectite abundances. *Clay Clay Miner.* **52**, 589–602.

Blum J. D. and Erel Y. (1997) Rb–Sr isotope systematics of a granitic soil chronosequence: the importance of biotite weathering. *Geochim. Cosmochim. Acta* **61**, 3193–3204.

Bradley W. C. and Griggs G. B. (1976) Form, genesis, and deformation of central California wave-cut platforms. *Geol. Soc. Am. Bull.* **87**, 433–449.

Brantley S. L., Bandstra J., Moore J. and White A. F. (2008) Modeling chemical depletion profiles in regoliths. *Geoderma* **145**, 494–504.

Brimhall G. H., Lewis C. J., Ford C., Bratt J., Taylor G. and Warin O. (1991) Quantitative geochemical approach to pedogenesis: importance of parent material reduction, volumetric expansion, and eolian influx in lateritization. *Geoderma* **51**, 51–91.

Bullen T., White A. F., Blum A., Harden J. and Schulz M. (1997) Chemical weathering of a soil chronosequence on granitoid alluvium: II. Mineralogic and isotopic constraints on the behavior of strontium. *Geochim. Cosmochim. Acta* **61**, 291–306.

Burch T. E., Nagy K. L. and Lasaga A. C. (1993) Free-energy dependence of albite dissolution kinetics at 80 °C and pH 8.8. *Chem. Geol.* **105**, 137–162.

Busenberg E. and Clemency C. V. (1973) Determination of cation exchange capacity of clays and soils using an ammonia electrode. *Clays Clay Miner.* **21**, 213–217.

Chadwick O. A., Hendricks D. M. and Nettleton W. D. (1987) Silica in duric soils I. A depositional model. *Soil Sci. Soc. Am. J.* **51**, 975–982.

Chadwick O. A., Brimhall G. H. and Hendricks D. M. (1990) From black box to a grey box: a mass balance interpretation of pedogensis. *Geomorphology* **3**, 369–390.

Chadwick O. A., Gavenda R. T., Kelly E. F., Ziegler K., Olson C. G., Elliott W. C. and Hendricks D. M. (2003) The impact of climate on the biogeochemical functioning of volcanic soils. *Chem. Geol.* **202**, 195–223.

Cleaves E. T. (1993) Climatic impact on isovolumetric weathering of a coarse-grained schist in the northern Piedmont Province of the central Atlantic states. *Geomophology* **8**, 191–198.

Coppin F., Berger G., Bauer A., Castet S. and Loubet M. (2002) Sorption of lanthanides on smectite and kaolinte. *Chem. Geol.* **182**, 57–68.

Corbin J. D., Thomsen M. A., Dawson T. E. and D'Antonino C. M. (2005) Summer water use by California coastal prairie grasses: fog, drought, and community composition. *Ecophysiology* **145**, 511–521.

Deer, W. A., Howie, R. A. and Zussman, M. A. (2001) *Rock-Forming Minerals*. 2nd ed., The Geological Soc., London, 971p.

Driscoll C. T., van Breemen N. and Mulder J. (1985) Aluminum chemistry in a forested spodosol. *Soil Sci. Soc. Am. J.* **49**, 437–444.

Driscoll C., Fallon-Lambert K. and Chen L. (2005) Acidic deposition: sources and effects. In *Encyclopedia of Hydrological Sciences* (ed. M. G. Anderson). John Wiley and Sons, NY, pp. 1–13.

Egli M. and Fitze P. (2000) Formulation of pedologic mass balance based on immobile elements: a revision. *Soil Sci.* **165**, 437–443.

Gaston L. A. and Selim (1991) Predicting cation mobility in kaolinitic media based on exchange selectivities of kaolinite. *Soil Sci. Am. J.* **55**, 1255–1261.

Gautier J. M., Oelkers E. H. and Schott J. (1994) Experimental study of K-Feldspar dissolution rates as a function of chemical affinity at 150-degrees-C and pH-9. *Geochim. Cosmochim. Acta* **58**, 4549–4560.

Gong S. L., Barrie L. A., Prospero M., Savoie D. L., Ayers G. P., Blanchet J. P. and Spacek L. (1997) Modeling sea-salt aerosols in the atmosphere: atmospheric concentrations and fluxes. *J. Geophys. Res.* **102**, 3819–3830.

Gustafsson M. E. R. and Franzen L. G. (2000) Land transport of marine aerosols in southern Sweden. *Atmos. Environ.* **34**, 313–325.

Hellmann R. and Tisserand D. (2006) Dissolution kinetics as a function of the Gibbs free energy of reaction: an experimental study based on albite feldspar. *Geochim. Cosmochim. Acta* **70**, 364–383.

Hodson M. E. and Langan S. J. (1999) The influence of soil age on calculated mineral weathering rates. *Appl. Geochem.* **14**, 387–394.

Kirkwood S. E. and Nesbitt H. W. (1991) Formation and evolution of soils from an acidified watershed: plastic Lake, Ontario, Canada. *Geochim. Cosmochim. Acta* **55**, 1295–1308.

Kistler R. W. and Champion D. E. (2001) Rb–Sr whole rock and mineral ages, K-Ar, $^{40}Ar/^{39}Ar$, and U–Pb mineral ages and strontium, lead, neodymium, and oxygen isotopic compositions for granitic rocks from the Salinian composite terrain, California. *U.S. Geol. Sur. Open-File Rep.* **01–453**, 84.

Kumao A., Nissen H. U. and Wessecken R. (1987) Structure images and superstructure model of calcic plagioclase. *Acta Cryst.* **B43**, 326–333.

Lebedeva M. J., Flecher R. C., Ballashov V. N. and Brantley S. L. (2007) A reactive diffusive model describing transformation of bedrock to saprolite. *Chem. Geol.* **244**, 624–645.

Lichtner P. C. (1988) The quasi-steady state approximation to coupled mass transport and fluid-rock interaction in a porous media. *Geochim. Cosmochim. Acta* **52**, 143–156.

Ma C. and Eggletton R. A. (1999) Cation exchange capacity of kaolinite. *Clay Clay Miner.* **47**, 174–180.

Maher K., DePalo D. J., Conard M. E. and Serne R. J. (2003) Vadose zone infiltration rate at Hanford, Washington, inferred from Sr isotope measurements. *Water Resources Research* **39**, SBH31–SBH314.

Maher K., Steefel C. I., DePaolo D. J. and Viani B. E. (2006) The mineral dissolution rate conundrum: Insights from reactive transport modeling of U isotopes and pore fluid chemistry in marine sediments. *Geochim. Cosmochim. Acta* **70**, 337–363.

Maher K., Steelel C. I., White A. F. and Stonestrom D. A. (2009) The role of reaction affinity and secondary minerals in regulating chemical weathering rates at the Santa Cruz Soil Chronosequence, California. *Geochimica et Cosmochimica Acta* **73**(10), 2804–2831.

Nagy K. L. and Lasaga A. C. (1993) Simultaneous precipitation kinetics of kaolinite and gibbsite at 80 °C and pH 3. *Geochim. Cosmochim. Acta* **57**, 4329–4335.

Nesbitt H. W., Fedo C. M. and Young G. M. (1997) Quartz and feldspar stability, steady and non steady state weathering and petrogenesis of siliciclastic sands and muds. *J. Geol.* **105**, 173–191.

Olsen A. (1974) Schiller effects and exsolution in sodium-rich plagioclases. *Contr. Miner. Petrol.* **47**, 141–152.

Ortoleva P., Chadam J., Merino E. and Sen A. (1987) Geochemical self-organization II. The reactive infiltration instability. *Am. J. Sci.* **287**, 1008–1040.

Parkhurst D. L. and Appelo C. A. J. (1999) User's guide to PHREEQC (version 2)—a computer program for the speciation, batch-reaction, one dimensional transport, and inverse geochemical calculations. *U.S. Geol. Sur. Water Resources Invest. Rept.* **99–4259**, 299p.

Parsons I. and Lee M. R. (2005) Minerals are not just chemical compounds. *Can. Miner.* **43**, 1959–1992.

Pavich M. J. (1986) Processes and rates of saprolite production and erosion on a foliated granitic rock of the Virginia Piedmont. In *Rates of Chemical Weathering of Rocks and Minerals* (eds. S. Coleman and D. Dethier). Academic Press, Orlando, pp. 551–590.

Perg L. A., Anderson R. S. and Finkel R. C. (2001) Use of a new ^{10}Be and ^{26}Al inventory method to date marine terraces, Santa Cruz, California, USA. *Geology* **29**, 879–882.

Perg L. A., Anderson R. S. and Finkel R. C. (2003) Use of cosmogenic radionuclides as a sediment tracer in the Santa Cruz littoral cell, California, United States. *Geology* **31**, 299–302.

Peterson J. R. and Coleman N. T. (1965) Active sorption of magnesium ions by vermiculite. *Soil Sci. Am. J.* **29**, 327–328.

Pokrovsky O. S., Dupré B. and Schott J. (2005) Fe–Al–organic colloids control of trace elements in peat soil solutions: results of ultrafiltration and dialysis. *Aquat. Geochem.* **11**, 241–278.

Ralph F. M., Neiman P. J., Kingsmill D. E., Perrsson P. O. G., White A. B., Stem E. T., Andrews E. D. and Antweiller R. C. (2003) The impact of a prominent rain shadow on flooding in California's Santa Cruz Mountains: a CALJET case study and sensitivity to the ENSO cycle. *J. Hydrometeorol.* **4**, 1243–1264.

Riebe C. S., Kirchner J. K. and Finkel R. C. (2003) Long-term rates of chemical weathering and physical erosion from cosmogenic nuclides and geochemical mass balance. *Geochim. Cosmochim. Acta* **67**, 4411–4427.

Rossnecht G. P., Elliot W. C. and Ramsey F. L. (1973) The size distribution and inland penetration of sea-salt particles. *J. Appl. Meteorol.* **12**, 825–830.

Smith, J. V. and Brown, W. L. (1988) *Feldspar Minerals, Crystal Structures, Physical, Chemical and Microtextural Properties.* 2nd ed., Springer, Berlin, 634p.

Sposito G., Holtzclaw K. M., Jouany C. and Charent L. (1983) Cation selectivity in sodium-calcium, sodium-magnesium and calcium-magnesium exchange on Wyoming bentonite at 298 K. *Soil Sci. Am. J.* **47**, 917–921.

Stonestrom D. A., White A. F. and Akstin K. C. (1998) Determining rates of chemical weathering in soils-solute transport versus profile evolution. *J. Hydrol.* **209**, 331–345.

Steefel C. I. and Van Cappellen P. (1990) A new kinetic approach to modeling water-rock interaction: the role of nucleation, precursors and Ostwald ripening. *Geochim. Cosmochim. Acta* **54**, 2657–2677.

Taylor A., Blum J. D. (1995) Relation between soil age and silicate weathering rates determined from the chemical evolution of a glacial chronosequence. *Geology* **23**, 979–982.

Varadahi C. (2006) Fuzzy phase diagrams of clay minerals. *Clays Clay Miner.* **54**, 616–625.

White A. F. (1995) Chemical weathering rates in soils. In Chemical Weathering Rates of Silicate Minerals, (eds. A. F. White and S. L. Brantley), *Reviews in Mineralogy* **31**, 407–458.

White A. F. (2002) Determining mineral weathering rates based on solid and solute weathering gradients: application to biotite weathering in saprolites. *Chem. Geol.* **190**, 69–89.

White A. F. (2008) Quantitative approaches to characterizing chemical weathering rates. In *Kinetics of Water-Rock Interac-*

tions (eds. S. L. Brantley, J. Kubicki, and A. F. White), Springer, pp. 467–532.

White A. F. and Brantley S. L. (2003) The effect of time on the weathering of silicate minerals: why do weathering rates differ in the laboratory and field? *Chem. Geol.* **202**, 479–506.

White A. F., Blum A. E., Schulz M. S., Bullen T. D., Harden J. W. and Peterson M. L. (1996) Chemical weathering of a soil chronosequence on granitic alluvium 1. Reaction rates based on changes in soil mineralogy. *Geochim. Cosmochim. Acta* **60**, 25333–25550.

White A. F., Blum A. E., Schulz M. S., Vivit D. V., Larsen M. and Murphy S. F. (1998) Chemical weathering in a tropical watershed, Luquillo Mountains, Puerto Rico: I. Long-term versus short-term chemical fluxes. *Geochim. Cosmochim. Acta* **62**, 209–226.

White A. F., Blum A. E., Stonestrom D. A., Bullen T. D., Schulz M. S., Huntington T. G. and Peters N. E. (2001) Differential rates of feldspar weathering in granitic regoliths. *Geochim. Cosmochim. Acta* **65**, 845–869.

White A. F., Blum A. E., Schulz M. S., Huntington T. G., Peters N. E. and Stonestrom D. A. (2002) Chemical weathering of the Panola Granite: solute and regolith elemental fluxes and the dissolution rate of biotite. In *Water-rock Interaction, Ore Deposits, and Environmental Geochemistry: A tribute to David A. Crerar*, Special Publ. no. 7 (eds. R. Hellmann and S. A. Wood). The Geochemical Society, pp. 37–59.

White A. F., Schulz M. S., Vivit D. V., Blum A. E., Stonestrom D. A. and Harden J. (2005) Chemical weathering rates of a soil chronosequence on granitic alluvium: part III. Hydrochemical evolution and contemporary solute fluxes and rates. *Geochim. Cosmochim. Acta* **69**, 1975–1996.

White A. F., Schulz M. S., Vivit D. V., Blum A. E., Stonestrom D. A. and Anderson S. P. (2008) Chemical weathering of a marine chronosequence, Santa Cruz, California I. Interpreting rates and controls based on soil concentration–depth profiles. *Geochim. Cosmochim. Acta* **72**, 36–68.

Yang L. and Steefel C. I. (2008) Kaolinite dissolution and precipitation at 22 °C and pH 4. *Geochim. Cosmochim.* **72**, 99–116.

Associate editor: Jacques Schott